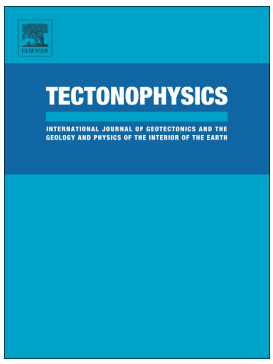

The closure of the Rocas Verdes Basin and early tectono-metamorphic evolution of the Magallanes Fold-and-Thrust Belt, southern Patagonian Andes (52–54°S)

A.P. Muller Veleda, Calderón Mauricio, C. Fosdick Julie, C. Ghiglione Matias, F. Cury Leonardo, Massonne Hans-Joachim, M. Fanning Christopher, J. Warren Clare, Ramírez de Arellano Cristobal, Sternai Pietro

PII: S0040-1951(20)30369-3

DOI: https://doi.org/10.1016/j.tecto.2020.228686

Reference: TECTO 228686

To appear in: *Tectonophysics*

Received date: 4 June 2020

Revised date: 24 October 2020

Accepted date: 29 October 2020

Please cite this article as: A.P. Muller Veleda, C. Mauricio, C. Fosdick Julie, et al., The closure of the Rocas Verdes Basin and early tectono-metamorphic evolution of the Magallanes Fold-and-Thrust Belt, southern Patagonian Andes (52–54°S), *Tectonophysics* (2020), https://doi.org/10.1016/j.tecto.2020.228686

T[illegible]d-and-Thrust Belt, southern Patagonian Andes (52-54°S)

Muller, Veleda A.P.[a,b,*] v.paivamuller@campus.unimib.it, Calderón, Mauricio[c] mauricio.calderon@unab.cl, Fosdick, Julie C.[d] julie.fosdick@uconn.edu, Ghiglione, Matias C.[e] matias@gl.fcen.uba.ar, Cury, Leonardo F.[a] cury@ufpr.br, Massonne, Hans-Joachim[f,g] h-j.massonne@mineralogie.uni-stuttgart.de, Fanning, Christopher M.[h] mark.fanning@anu.edu.au, Warren, Clare J.[i] clare.warren@open.ac.uk, Ramírez de Arellano, Cristobal[c] cristobal.ramirez@unab.cl, Sternai, Pietro[b] pietro.sternai@unimib.it

[a]Laboratório de Análise de Minerais e Rochas, Departamento de Geologia da Universidade Federal do Paraná, Av. Cel. Francisco H. dos Santos 210, Curitiba, Brazil.

[b]Dipartimento di Scienze dell'Ambiente e della Terra, Università degli Studi di Milano-Bicocca, Piazza della Scienza 4, Milan, Italy.

[c]Carrera de Geología, Facultad de Ingeniería, Universidad Andres Bello, Sazié 2119, Santiago, Chile.

[d]Department of Geosciences, University of Connecticut, 354 Mansfield Road, U-1045, Storrs, Connecticut 06269, USA.

[e]Instituto de Estudios Andinos "Don Pablo Groeber", Universidad de Buenos Aires, CONICET, Buenos Aires, Argentina.

[f]School of Earth Sciences, China University of Geosciences, Lumo Road 388, 430074 Wuhan, China

[g]Fakultät Chemie, Universität Stuttgart, Pfaffenwaldring 55, D-70174 Stuttgart, Germany.

[h]Research School of Earth Sciences, Australian National University, Canberra, Australia.

[i]School of Environment, Earth & Ecosystem Sciences, The Open University, Milton Keynes MK7 6AA, United Kingdom

[*]Corresponding author.

1.1 Abstract:

The hinterland *Western Domain* of the Magallanes Fold-and-Thrust Belt (MFTB) between 52°-54°S is part of a poorly studied region of the southernmost Andean Cordillera. This domain consists of NNW-SSE trending tectonic slices of pre-Jurassic basement units and Late Jurassic-Early Cretaceous ophiolitic complexes and volcano-sedimentary successions of the Rocas Verdes Basin (RVB). New detrital zircon U-Pb ages of metatuffs and metapsammopelites constrain episodes of Late Jurassic rift-related volcanism (ca. 160 Ma) followed by Early Cretaceous sedimentation (ca. 125 Ma) during the opening of the RVB. Shear bands developed in the RVB units further record the initial phases of the Andean Orogeny. The 30-km wide thrust stack located on top of the *Eastern Tobífera Thrust* consists of mylonitic metatuffs, metapelites and metabasalts with a NE-verging brittle-ductile S_1* foliation. Phengite-bearing metatuffs commonly record pressure-temperature (P-T) conditions between ~ 3-6 kbar and ~ 210-460°C, consistent with underthrusting of the RVB beneath the parautochthonous magmatic arc in the west. Peak metamorphic conditions of ~ 6 kbar and 460°C are derived from a metapsammopelitic schist with textures of contact metamorphism overprinting early mylonitic structures (at least S_1*). A back-arc quartz-diorite, intruded at ca. 83 Na, is in contact with the metapsammopelites and constrain the minimum age of deformation at deep crustal depths. Campanian-Maastrichtian (ca. 70-73 Ma) $^{40}Ar/^{39}Ar$ phengite dates from a mylonitic metapelite indicate the timing of thrusting and backthrusting during the initial uplift of the underthrusted crustal stack. These findings reveal a ~ 400 km along-strike connection of mylonite belts in a continent-verging thrust structure that became active at the onset of the Andean orogeny during the closure of the Rocas Verdes back-arc marginal basin.

KEYWORDS: Rocas Verdes Basin; Patagonian Andes; fold-and-thrust belt; shear zones.

1.2 1. Introduction

The Andes constitute the archetype of a subduction-related orogen, where compressional stresses due to ocean-continent subduction control mountain building throughout shortening and thickening of the upper continental lithosphere (Dewey and Bird, 1970; Dalziel, 1986; Ramos, 1999; Schellart, 2008; Horton et al., 2018). However, extensional stresses were dominant during Gondwana tectonic dispersal in the early Mesozoic (Cox, 1992, Pankhurst et al., 1998; Dalziel et al., 2013; Braz et al., 2018). At this time, Pacific marginal and back-arc basins opened, leading to seafloor spreading at the northern and southern tips of South America (Dalziel et al, 1974; Stern and De Wit, 2003; Braz et al., 2018) and development of tectonic environments similar to those in present-day East Asia (Schellart and Lister, 2005). Tectonic inversion and closure of a proto-oceanic basin in southernmost South America occurred in the Late Cretaceous, possibly due to accelerated spreading rates in the opening of the South Atlantic (Dalziel, 1981). This shift resulted in ophiolite-bearing thrust sheets emplaced on the South American continent (Dalziel et al., 1974, Klepeis et al., 2010; Calderón et al., 2012). These deformed remnants of back-arc basin lithosphere preserve the

st th America (Dalziel et al., 1974; Stern and De Wit, 2003; Kraemer, 2003; Calderón et al., 2007; Poblete et al., 2016).

The Andean fold-and-thrust belts are generally segmented along-strike, with thrust sheets involving just the sedimentary cover, versus those that include crystalline basement, known as thin- or thick-skinned sectors, respectively (Coward, 1983; Pfiffner, 2006; Lacombe and Bellahsen, 2016). The typical Andean configuration includes deeper (i.e., thick-skinned) structures to the west-hinterland, which became progressively shallow (i.e., thin-skinned) cratonward to the east. Commonly, initially thin-skinned sectors have been affected by re-activation of deep-seated structures and initiation of thick-skinned deformation (Lacombe and Bellahsen, 2016). Therefore, pre-Cenozoic inherited structures appear to have exerted a major control on the style of deformation during Andean crustal shortening (Winslow, 1982; Allmendinger et al., 1983; Kley et al., 1999; Ramos et al., 2004; Fosdick et al., 2011; Likerman et al., 2013). In this context, shear zones that developed at different crustal depths played an important role in accommodating contractional deformation during Andean orogenesis, and may have transferred shortening between different fold-and-thrust belt domains in a time-progressive construction (Price and McClay, 1981; Davis et al., 1983; Platt, 1986; Selzer et al., 2007). Estimates of pressure-temperature (P-T) conditions coupled to the study of the structures are crucial to resolving the polarity and depth of tectonic burial and exhumation of the fold-and-thrust belts (Ernst, 1972; Miyashiro, 1973; Platt, 1986; Jamieson et al., 1998; Ernst, 2005; Agard et al., 2009; Massonne and Willner, 2008; Jolivet et al., 2010).

This study focuses on the early history of the Andean Orogeny in southernmost Patagonia, where the changes in stress conditions from an extensional to compressive regime, thereby closing the proto-oceanic Late Jurassic-Early Cretaceous Rocas Verdes Basin (RVB, Dalziel et al., 1974). Remnants of this back-arc basin are currently exposed in the hinterland domain of the Magallanes Fold-and-Thrust Belt (MFTB), located to the east of the Patagonian Batholith (Fig. 1). Several paleogeographic models have been proposed to explain the closure and inversion of the RVB (Dalziel, 1981; Cunningham et al., 1991; Kraemer, 2003; Fildani and Hessler, 2005; Calderón et al., 2007; Rapalini et al., 2008, 2015; Klepeis, 2010; Calderón et al., 2012; Fosdick et al., 2011; Poblete et al., 2016; Eagles, 2016). This tectonic event resulted in the ~ 90° counter-clockwise rotation of the southern tip of South America, where the orogenic belts change in orientation from north-south to west-east, a feature known as the Patagonian Orocline (Cunningham et al., 1991; Kraemer, 2003; Rapalini et al., 2008; Poblete et al., 2016; Eagles et al., 2016). The onset of thrust loading of RVB units during its tectonic inversion promoted topographic loading of the foreland lithosphere and development of the Magallanes-Austral Basin to the east (Wilson, 1991; Fildani and Hessler, 2005; Romans et al., 2011; Fosdick et al., 2014). Generally, models agree that the RVB was closed by mid-Cretaceous time due to the relative motion of a microplate against the South American Plate (cf. Eagles, 2016). However, many fundamental aspects of this tectonic transition remain poorly known, including the plate kinematics, the consumption (or not) of the oceanic floor by a west-directed subduction, the mechanisms of basin shortening, and the overall timing of events. The segment under investigation connects the N-S oriented Patagonian Andes and the E-W oriented Fuegian Andes (52°-54°S, Fig. 1A), encompassing the Seno Skyring and Seno Otway (Fig. 2). This segment is less studied compared to the northern and southern parts of the deformed RVB.

We bring new regional and local structural observations, geochronology, and thermobarometry datasets to reconstruct the early history of the study region. The regional structure of the thick- and thin-skinned domains of the MFTB at this latitude is constructed from seismic-reflection data and surface exposure field data (Fig. 1 B). Stratigraphic and structural field observations allow construction of local cross sections at Canal Gajardo (Fig. 3 A) and Estero Wickham (Fig. 3 B), where initial east-vergent thin-skinned deformation is superimposed by thick-skinned deformation. New Sensitive High Resolution Ion Micro Probe (SHRIMP) U-Pb analyses in detrital zircons provide constraints on the timing of deposition of the volcanic and sedimentary units of the RVB. SHRIMP U-Pb zircon crystallization ages of dioritic plutons that cross-cut mylonitic rocks of the MFTB provide a bracket for the timing of deep ductile deformation, which correlates with the timing of tectonic emplacement of the *Sarmiento Ophiolitic Complex*. The P-T constraints obtained from silicic mylonites and metapsammopelitic schists allow us to estimate the tectonic

b of phengitic white mica from a mylonitic metapelite constrains the age of out-of-sequence thrusting and backthrusting in the hinterland *Western Domain* of the MFTB, which was responsible for the Late Cretaceous uplift of the orogenic belt. Based on these new data, we propose and discuss a geodynamic reconstruction of the along-strike exhumation history of the RVB units between the southern Patagonian and the Fuegian Andes.

1.3 2. Geological setting

1.4 2.1. Stratigraphy of the Magallanes-Fold-and-Thrust Belt

The early phase of Jurassic tectonic dispersal of Gondwanan landmasses was accompanied by the development of a wide volcanic rift zone in southwestern South America (Dalziel et al., 1974; Bruhn et al., 1978; Pankhurst et al., 1998, 2000). In this context, the inception of the RVB occurred in the Middle Jurassic by rifting of the pre-Jurassic basement complexes, which were overlain by Jurassic pyroclastic, volcaniclastic and sedimentary successions (Bruhn et al., 1978; Forsythe and Allen, 1980; Dalziel, 1981; Stern and De Wit, 2003, Calderón et al., 2007; Hervé et al., 2008, 2010a).

The continental basement in Patagonia comprises Paleozoic to early Mesozoic accretionary complexes of the proto-Pacific subduction zone (Nelson et al., 1980; Kohn et al., 1993; Hervé et al., 2003, 2008, 2010a; Hervé and Fanning, 2003; Willner et al., 2004; Hyppolito et al., 2016, Angiboust et al., 2017, 2018; Suárez et al., 2019). The Paleozoic-Early Triassic *Eastern Andes Metamorphic Complex* extends from the Ultima Esperanza region (~ 51°S) to the Estrecho de Magallanes (Fig. 1A), and consists of low-grade metapsammopelitic schists with minor intercalations of marbles and metabasic bodies (Forsythe and Allen, 1980; Allen, 1982; Hervé et al., 2003, Hervé et al., 2008; Bella et al., 2015). To the east, the basement of the Magallanes-Austral Basin consists of the high-grade *Tierra del Fuego Igneous and Metamorphic Complex* overlain by Jurassic rift-related silicic volcanic rocks (Hervé et al., 2010a). To the south of Estrecho de Magallanes, the Paleozoic-Mesozoic *Cordillera Darwin Metamorphic Complex* comprises medium to high-grade metapelitic schists, metabasalts, and Jurassic metarhyolites metamorphosed in the Late Cretaceous (Nelson et al., 1980; Kohn et al., 1993, 1995; Hervé et al., 2008; Hervé et al., 2010b; Klepeis et al., 2010, Maloney et al., 2011).

During the early rift-stage of the RVB the depocenters were filled with silicic lava flows, volcaniclastic successions (mostly tuffs and ignimbrites), and sedimentary fluxes of coarse- and fine-grained siliciclastic detritus belonging to the Tobífera Fm. (Fig. 2; Dalziel et al., 1974; Bruhn et al., 1978; Forsythe and Allen, 1980; Dalziel, 1981; Allen, 1982; Wilson, 1991; Pankhurst et al., 1998, 2000; Calderón et al., 2007). Rift volcanism and sedimentation lasted from ca. 170 to 140 Ma (Pankhurst et al., 2000; Calderón et al., 2007; Hervé et al., 2007a; Malkowski et al., 2015a) and fossiliferous siltstones (with ammonites, belemnites, and inoceramids) indicate a predominant submarine deposition during the Early Cretaceous (Allen, 1982; Fuenzalida and Covacevich, 1988; Wilson, 1991). Volcanism was partially coeval with the first phase of plutonism of the *South Patagonian Batholith*, represented by granites and gabbros of 157 to 144 Ma (Hervé et al., 2007a), which bounds the RVB to the west (Figs. 1 and 2).

Progressive lithospheric stretching within the back-arc region resulted in oceanic-type lithosphere formation along mid-ocean-ridge spreading centers, located between the South America cratonic margin and a microplate bearing the southwestern magmatic arc, represented by the Early Cretaceous components of the South Patagonian and Fuegian batholiths (Katz, 1964; Dalziel et al., 1974; Stern, 1979; Dalziel, 1981; Hervé et al., 1984; Stern and De Wit, 2003; Hervé et al., 2007a). In the southern Patagonian Andes, mafic and bimodal igneous suites were emplaced along-strike within the *Sarmiento Ophiolitic Complex* (Calderón et al., 2007; Fig. 1 A). The oceanic remnants consist of pillow and massive basalts with intercalations of cherts and siltstones, underlain by sheeted dyke complexes, minor gabbros and rare plagiogranites (Dalziel et al., 1974; Dalziel, 1981; Allen, 1982; Stern and De Wit, 2003; Calderón et al., 2007). In the Fuegian Andes, the northwestern edge of the Scotia Plate, these remnants are referred as the Tortuga and Capitan Aracena ophiolitic complexes (Fig. 1 A; Calderón et al., 2013).

The following regional sag phase of basin evolution constituted a Late Jurassic to Early Cretaceous marine transgression recorded by deposition of hemipelagic successions of the Zapata (Patagonian Andes), Erezcano (Isla Riesco) and Yaghan/Beauvoir (Fuegian Andes) formations, covering the ophiolitic and the

Calderón et al., 2007; McAtamney et al., 2011). These units are are dominated by shale-rich successions over ~ 1000 m in thickness in the Patagonian Andes, and nearly ~ 3000 m in thickness in the Fuegian Andes (Cortés, 1964; Suárez and Pettigrew, 1976; Allen, 1982; Wilson, 1991; Fildani and Hessler, 2005). The upper stratigraphic section bears intercalations of sandy turbidites that progressively increase in thickness towards the overlapping Canal Bertrand (Fig. 2; Mpodozis et al., 2007; McAtamney et al., 2011). The facies transition to turbidites is interpreted to reflect an increase in sediment supply and higher depositional energy linked to the beginning of Andean deformation, resulting in cratonward thrusting of the MFTB and subsidence in the east-foreland (Wilson, 1991; Harambour, 1998; Fildani et al., 2003, 2008; Fildani and Hessler, 2005; McAtamney et al., 2011; Malkowski et al., 2015b). These diachronous Aptian-Albian to Turonian maximum sedimentation ages delimitate the end of deposition in the RVB and onset of the foreland stage in the Magallanes-Austral Basin, from north to south (Fildani et al., 2003; Barbeau Jr. et al., 2009; Fosdick et al., 2011; Ghiglione et al., 2015; Malkowski et al., 2015b).

The Upper Cretaceous sedimentary successions of the Magallanes-Austral Basin vary stratigraphically along-strike due to changes in the geometry of the depocenters, controlled by the geometry of inherited extensional faults and the structural evolution of the fold-and-thrust belt (Winslow, 1982; Kraemer, 1998; Fildani and Hessler, 2005; Ghiglione et al., 2009; Bernhardt et al., 2011; Fosdick et al., 2011, McAtamney et al., 2011; Romans et al., 2011; Malkowski et al., 2015b). In the study area, the interface between the RVB and Magallanes-Austral Basin is generally dominated by sand-rich turbidites of the Canal Bertrand Fm. (Wilson, 1991; Fildani and Hessler, 2005; McAtamney et al., 2011), interbedded with mafic volcanic and volcaniclastic rocks of La Pera Complex (Stern et al., 1991; Prades, 2008; Anguita, 2010). These units are capped by deep marine shale-rich successions of the Latorre Fm. (Fig. 2; Mpodozis et al., 2007; McAtamney et al., 2011). The turbidites within the upper section of the Latorre Fm. represent the transition from hemipelagic sedimentation to deep-marine turbiditic clast-supported conglomerates of the Escarpada Fm., deposited at ca. 80 Ma (McAtamney et al., 2011). The overlying Maastrichtian Fuentes and Rocallosa formations, which consist of intercalated mudstones, sandstones, and limestones, record the transition from a shelf to deltaic environment (Charrier and Lahsen, 1969; Castelli et al., 1992; Mpodozis et al., 2007), reflecting the regional shallowing of the Magallanes-Austral Basin during the Late Cretaceous.

1.5 2.2. Structural segmentation of the Magallanes Fold-and-Thrust Belt

The MFTB can be divided into three main structural domains (Figs. 1 B and 3; after Alvarez-Marrón et al., 1993): (1) The *Western Domain*, which is the focus of this study, comprises Jurassic-Lower Cretaceous RVB units and pre-Jurassic basement complexes deformed by thick-skinned tectonics; (2) the *Central Domain*, which exposes Upper Cretaceous foredeep units of the Magallanes-Austral Basin within a thick-skinned system dominated by basement-involved inversion structures; and (3) the *Eastern Domain*, defined by outcropping Paleogene foredeep units of the Magallanes-Austral Basin, dominated by thin-skinned deformation.

The *Western Domain* transferred shortening towards the external domains by linking upper crustal thrust faults to deep detachment faults within the pre-Jurassic basement and near the top of the Tobífera Fm. (Alvarez-Marrón, 1993; Harambour, 2002; Kraemer, 2003; Klepeis et al., 2010; Fosdick et al., 2011; Betka et al., 2015). East-vergent detachment faults formed in the earliest Late Cretaceous due to inversion of the RVB, accommodated 30-40 km of shortening of the MFTB in the Patagonia sector (Fosdick et al., 2011; Betka et al., 2015) and 50-100 km of shortening in the Fuegian sector (Kohn et al., 1995; Klepeis et al., 2010; Rojas and Mpodozis, 2006). This phase may have included partial consumption of the proto-oceanic lithosphere by west-directed subduction (Kraemer, 2003). Out-of-sequence thrusting and backthrusting within the RVB succession may have initiated in the Late Cretaceous and continued throughout the Paleogene, leading to deformation of the Upper Cretaceous foreland units of the Magallanes-Austral Basin (Kohn et al., 1995; Harambour, 2002; Kraemer, 2003; Rapalini et al., 2008; Klepeis et al., 2010; Fosdick et al., 2011; Betka et al., 2015). Inversion of inherited-basement faults from the rift phase is taken as an important uplift mechanism during this phase (Winslow, 1982; Alvarez-Marron, 1993; Harambour, 2002; Kraemer, 2003; Rapalini et al., 2008; Fosdick et al., 2011; Likerman et al., 2013; Betka et al., 2015). From

th ut led to overall less shortening and lower foreland propagation rates (Fosdick et al., 2011). Along the margins of the thrust domains, shallow thrusts rooted in the pre-Jurassic -Tobífera Fm. interface (Fig. 1 B) exhibit a forward-breaking sequence (Alvarez-Marrón et al., 1993), and contributed to exhumation of the MFTB (Fosdick et al., 2011, 2013) .

1.5.12.2.1) Western Domain of the MFTB

The Upper Jurassic Rocas Verdes ophiolites show mutual cross-cutting relationships with the intrusive bodies of the *South Patagonian Batholith* in the westernmost part of the MFTB (Dalziel, 1981; Stern and De Wit, 2003; Hervé et al., 2007a; Calderón et al., 2007). North of the study zone in the Cordillera Sarmiento (~ 51-52°S; Fig. 1 A), the *Canal de las Montañas Shear Zone* places the ophiolites in thrust contact with the Zapata and Tobífera formations, resulting in a regional cratonward tectonic vergence (Calderón et al., 2012). This km-wide shear zone is defined by mylonitic metatuffs, metapelites and metabasalts derived from the RVB volcano-sedimentary successions. The P-T metamorphic constraints recorded in felsic mylonites of ~ 250-400°C and ~ 5-7 kbar are addressed to a phase of underthrusting of the oceanic and thinned continental lithosphere of the RVB before ca. 85 Ma (Calderón et al., 2012). In the Fuegian Andes (~ 54-56°S) the Tortuga and Capitan Aracena ophiolitic complexes are thrusted over the basement and volcano-sedimentary units of the RVB, and intruded by several back-arc plutons at ca. 90-80 Ma (Fig. 1 A; Nelson et al., 1980; Hervé et al., 1984; Cunningham, 1995; Klepeis et al., 2010; Calderón et al., 2013).

The mylonitic belts within the RVB successions are cross-cut by out-of-sequence cratonward thrusts and trenchward backthrusts, dated between ca. 70 and 40 Ma (Kohn et al., 1995; Harambour, 2002; Kraemer, 2003; Rapalini et al., 2008; Klepeis et al., 2010; Fosdick et al., 2011; Maloney et al., 2011; Betka et al., 2015). The trench-parallel imbricated arrangement of the *Western Domain* of the MFTB is constituted by structural duplexes of the Tobífera and Zapata formations, tectonically intercalated with the pre-Jurassic basement complexes (Allen, 1982; Fosdick et al., 2011; Calderón et al., 2012). The apatite and zircon fission tracks and (U-Th)/He cooling ages show a protracted history of deep exhumation of the *Western Domain* of the MFTB until the Miocene (Thomson et al., 2001; Fosdick et al., 2013).

In the Fuegian Andes, the *Cordillera Darwin Metamorphic Complex* comprises high-grade kyanite- and garnet-bearing schists, Jurassic orthogneisses and metamorphosed volcano-sedimentary rocks of the RVB (Hervé et al., 2010b; Klepeis et al., 2010). Metamorphic petrology and geochronological studies indicate that the metamorphic complexes were buried to ~ 35 km depths, during collision of the parautochthonous magmatic arc against the South American continental margin, before ca. 73 Ma (Dalziel, 1986; Kohn et al., 1993, 1995; Cunningham, 1995; Klepeis et al., 2010; Maloney et al., 2011). The exhumation is interpreted to have resulted from a late deep-seated thrusting phase in the Paleogene (Nelson, 1982; Kohn et al., 1995; Klepeis et al., 2010; Maloney et al., 2011).

1.5.22.2.2) Central Domain of the MFTB

The *La Pera Thrust* fault places the Zapata Fm. onto the Upper Cretaceous volcano-sedimentary rocks of the Canal Bertrand, Latorre, and Escarpada formations (Fig. 1 A and B; Mpodozis et al., 2007; McAtamney et al., 2011). The Upper Cretaceous units record east-verging thrusts and open-to-closed folds of regional scale, gradually decreasing in amplitude from west to east.

Seismic surveys across the *Central Domain* show the west-to-east structural transition from inverse steep, east-verging faults to high-angle west-and-east dipping normal faults rooted in the pre-Jurassic basement, which seemingly represent deep-seated inherited horst-graben structures (Winslow, 1982; Wilson, 1991; Harambour, 1998; Fosdick et al., 2011; Likerman et al., 2013; Betka et al., 2015).

1.5.32.2.3) Eastern Domain of the MFTB

The *Rocallosa Thrust* bounds the Central and Eastern domains, defining the transition between thick-skinned to predominantly thin-skinned deformation (Fig. 1 B). The *Eastern Domain* comprises the Upper Cretaceous Fuentes and Rocallosa formations, both of which are affected by shallow thrust faults, and the

w 999; McAtamney et al., 2011; Betka et al., 2015).

1.6 3. Methods

1.7 3.1. Structural and petrographic analysis

Field descriptions were collected from 36 outcrops to the west of Seno Otway and Seno Skyring (Fig. 2). Analysis of 70 thin sections yielded the determination of the mineral assemblages, textures, and microstructures in different samples belonging to the West and Central domains of the MFTB; 9 of these thin section samples were oriented to determine microscopic kinematic shear sense indicators (Table 1).

The structural data of foliations, lineations, and volcano-sedimentary bedding were plotted in stereographic diagrams, at equal-angle projections (Fig. 3), and in the geological map of Fig. 2 complemented with previously published geological and structural data (SERNAGEOMIN, 2003; Betka, 2013).

The structural cross section of the MFTB of Fig. 1 B is based on field data and 2-D seismic surveys done by ENAP (cf. Harambour, 1998). The structural cross section at Canal Gajardo (Fig. 3 A) and Estero Wickham (Fig. 3 B) are proposed on the basis of new field and geochronological data and data from previous works (Harambour, 2002; Betka et al., 2015).

1.8 3.2. SHRIMP zircon U-Pb geochronology

In an attempt to constrain the maximum depositional age of the different tectonic slices of the *Western Domain* of the MFTB, zircon grains have been separated from a silicic metatuff of the Tobífera Fm. (FC1727) at Estero Wickham, and a metapsammopelitic rock of the Zapata Fm. (FC1754) at Canal Gajardo. To constrain a relative age of deformation in RVB units, zircon grains were separated from a quartz-diorite pluton (FC1759) intruding the Tobífera and Zapata thrust sheets in Canal Gajardo (Figs. 2 and 3 A). The U-Pb analyses were carried out using SHRIMP II (FC1727 and FC1759; six scan data) and SHRIMP RG (FC1754; four scan data) at the Research School of Earth Sciences, Australian National University, in Canberra. Analytical techniques essentially follow those given in Williams (1998), the U/Pb ratios calibrated using analyses of the Temora reference zircon (Black et al, 2003). The data have been processed using the SQUID Excel Macro of Ludwig (2000) with corrections for common Pb made using the measured $^{238}U/^{206}Pb$ and $^{207}Pb/^{206}Pb$ ratios following Tera and Wasserburg (1972) as outlined in Williams (1998); see Table 2 A-C. Uncertainties in weighted mean age calculations are reported at the one σ level. The geological time-scale used follows the Chronostratigraphic Chart 2018 by IUGS-ICS (www.stratigraphy.org).

1.9 3.3. $^{40}Ar/^{39}Ar$ geochronology

To constrain the age of deformation in the *Western Domain* of the MFTB, up to 500 μm-long and 100 μm-wide phengite mats (mix of crystals) from a mylonitic metapelite of the Zapata Fm. (SHP141) in Canal Gajardo (Fig. 2) were analyzed by *in situ* $^{40}Ar/^{39}Ar$ analysis. The in-situ dating provides textural control, and the range of yielded ages provide insights into the metamorphic and structural evolution of the sample. The analysis was performed in the Open University $^{40}Ar/^{39}Ar$ Laboratory. Polished thick sections of this sample were broken into 5x5 mm^2 squares, washed in acetone and distilled water before packing into foil packets, and air dried at ambient temperature. Mica mats were analyzed by spot-dating using an SPI SP25C 1090 nm laser focused through a Leica microscope, coupled to an automated extraction system and a Nu Noblesse mass spectrometer; laserprobe diameter is 50 μm. Neutron fluency was monitored using the GA1550 biotite standard with an age of 98.79 ± 0.54 Ma (Renne et al., 1998). J values were calculated by linear interpolation between two bracketing standards (and given in Table 3); a standard was included between every 8 and 10 samples in the irradiation tube. Results were corrected for blanks, ^{37}Ar decay and neutron-induced interference reactions. Typical blank measurements are included for each sample and sample run in Table 3; tabled data are blank corrected. Background measurements bracket every 1–2 spots. The correction factors used were: $(^{39}Ar/^{37}Ar)Ca=0.00065$, $(^{36}Ar/^{37}Ar)Ca=0.000265$, $(^{40}Ar/^{39}Ar)K=0.0085$ based on analyses of Ca and K salts. Analyses were also

major-element composition of white mica crystals was measured with the electron probe micro analyzer, described below.

1.10 3.4. Bulk-rock X-ray fluorescence spectrometry

Three silicic metatuffs of the Tobífera Fm. (FC1723, FC1727, and FC1749) and one metapsammopelite of the Zapata Fm. (FC1757) were selected to constrain the P-T conditions of metamorphism at different structural levels within the MFTB (Fig. 2) through the construction of phase diagrams (cf. Massonne and Willner, 2008). The whole rock major-element composition was determined with a PHILIPS PW 2400 X-ray fluorescence (XRF) spectrometer at Universität Stuttgart, using glass discs prepared from rock powder and Spectromelt®. The results are presented in Table 4. The procedures of thermodynamic modeling are described below (section 3.6). All samples show dynamic recrystallization and syntectonic growth of very fine-grained white mica and chlorite defining the main foliation. A brief petrographic description of mineral assemblages and textures is provided in section 4.2.

1.11 3.5. Mineral analyses with the electron probe micro analyzer (EPMA)

We analyzed the major-element compositions of phengite, chlorite, epidote, feldspar, and biotite present in four selected samples. The white mica composition on sample SHP141 was also analyzed to discuss the meaning of $^{40}Ar/^{39}Ar$ *in situ* dating. The mineral chemical composition was determined using the EPMA CAMECA SX100 at Universität Stuttgart, with 5 wavelength-dispersive spectrometers and an energy-dispersive system. Operating conditions were an acceleration voltage of 15 kV, a beam current of 15 nA, a beam size of 1–3 µm or a focused beam (for very small crystals), and 20 seconds counting time on the Kα peak (Ba: Lα) and on the background for each element. The standards used were natural wollastonite (Si, Ca), natural orthoclase (K), natural albite (Na), natural rhodonite (Mn), synthetic Cr_2O_3 (Cr), synthetic TiO_2 (Ti), natural hematite (Fe), natural baryte (Ba), synthetic MgO (Mg), synthetic Al_2O_3 (Al) and synthetic NiO (Ni). The PaP correction procedure provided by CAMECA was applied. Analytical errors of this method are given by Massonne (2012). Representative mineral compositions are given in Table 5.

1.12 3.6. Thermodynamic modeling

P-T isochemical phase diagrams (i.e., pseudosections) contoured by isopleths regarding the chemical composition and modal contents of syntectonic minerals (e.g. white mica, chlorite, epidote) were calculated using the software package PERPLE_X 6.8.0 (cf. Connolly, 1990) to constrain P-T conditions of regional metamorphism in the four selected samples. We used the thermodynamic input parameters provided by Holland and Powell (1998, updated 2002) for minerals and aqueous fluids. The solid-solution models, selected from those included in PERPLE_X 6.8.0, were by (1) Holland et al. (1998): Chl(HP) for chlorite; (2) Holland and Powell (1998): Ctd(HP) for chloritoid, Ep(HP) for epidote, Gt(HP) for garnet, Omph(HP) for Na-bearing clinopyroxene, Pheng(HP) for potassic white micas, TiBio(HP) for biotite; (3) Massonne and Willner (2008) and Massonne (2010): Act (M) for actinolite, Mica(M) for paragonite, Stlp(M) for stilpnomelane, Carp(M) for carpholite, Pu(M) for pumpellyite; (4) Fuhrman and Lindsley (1988): feldspar for plagioclase and alkali feldspar; and (5) Andersen and Lindsley (1988): MtUl(A) for ulvospinel and magnetite. The model IlGkPy for ilmenite-geikielite-pyrophanite is based on ideal mixing of the three end members. The calculated mineral assemblages for the analyzed samples are shown in Table 6 with the respective modal compositions.

1.13 4. Results

In the study region, the NNW-SSE-trending thrust sheets of volcano-sedimentary rocks of the Tobífera and Zapata formations are imbricated to the northeast in a cratonward thrust wedge, with variably shallow to steep dip angles. The tectonic repetition of the Tobífera Fm. over the older Zapata Fm. is characteristic of duplex structures in the *Western Domain* of the MFTB. The hanging wall of the easternmost duplex of the *Western Domain*, the *Eastern Tobífera Thrust* (Figs. 2 and 3) is characterized by moderately strained phengite-bearing mylonites suitable for P-T metamorphic constraints. To the east, the

formations along the *La Pera Thrust*.

The ophiolitic complexes consist of tectonic slices of pillow basalts and foliated metabasalts intercalated within the Tobífera thrust sheets at Canal Gajardo. The pre-Jurassic basement rocks are thrust onto Tobífera thrust sheets. Plutonic rocks of the *South Patagonian Batholith* are located to the west of the MFTB, and satellite plutons cross-cut the MFTB (Figs. 2 and 3).

Metamorphic/mylonitic foliations S_1* and S_2* in the Tobífera and Zapata formations and *Sarmiento Ophiolitic Complex* are distinguished by an asterisk (*) to separate them from S_1 and S_2 foliations of the pre-Jurassic basement rocks because they may have different tectonic origin. However, S_1* in RVB units and S_2 in the pre-Jurassic basement are related to the same tectonic event, as discussed below.

1.14 4.1. Mesoscale Structures

In the westernmost area of Canal Gajardo, a thrust sheet containing the Zapata Fm. consists of metapsammopelitic rocks with a S_1* foliation crenulated by mm-to-cm closed folds. An axial planar S_2* foliation is NW-SE-striking and dips ~ 70° to the northeast. These rocks are thrust over crenulated silicic metatuffs and metapsammitic rocks of the Tobífera Fm. and show a NW-SE-trending S_1* foliation dipping between 40° and 80° to the west and to the east (Figs. 2 and 3 A1). The doubly dipping structure of S_1* is due to open folds with tens of meters wavelength.

The greenish foliated metabasalts of the *Sarmiento Ophiolitic Complex* in the western area of Canal Gajardo show a NW-SE-striking S_1* schistosity, variably dipping ~ 15-20° either to the southwest and northeast (Figs. 2 and 3 A1). To the east, a thrust sheet containing silicic metatuffs of the Tobífera Fm. is backthrust over the ophiolites by NW-SE-striking fault zones that dip 45° to the northeast. Further east the S_1* foliation in metatuffs dips to the southwest. These rocks are thrust over a second tectonic slice of mafic rocks of the *Sarmiento Ophiolitic Complex* (Figs. 2 and 3 A1), constituted of metabasalts with locally preserved pillow structures of up to 30 cm diameter, interleaved within metatuffs of the Tobífera Fm. (Figs. 2 and 3 A1).

To the east of the ophiolitic slices in the central area of Canal Gajardo, metarhyolites, silicic metatuffs, and shales of the Tobífera Fm. are thrust onto mylonitic metapsammopelitic rocks of the Zapata Fm. (Figs. 2 and 3 A1), resembling the geometry of an imbricated duplex. The metapsammopelitic rocks show a crenulated NW-SE-striking S_1* foliation that dips ~ 25° to the southwest (e.g. FC1754). Near satellite quartz-diorite plutons (e.g. FC1759; Figs. 2 and 3 A1) the S_1* foliation in metasedimentary rocks is overprinted by a hornfels texture possibly generated by contact metamorphism (e.g. FC1757).

At the central area of Canal Gajardo the western Zapata and Tobífera duplex is thrust over a tectonic slice of the pre-Jurassic basement complexes (Figs. 2 and 3 A2). The pre-Jurassic basement rocks consist of metapsammopelitic schists (e.g. FC1753) with an early S_1 foliation tightly folded by an up to 5 cm wavelength asymmetric crenulation cleavage S_2 that may present a S-C geometry. The S_2 foliation strikes NNW-SSE and dips ~ 25-50° to the southwest (Figs. 2 and 3 A2), being subparallel to the metamorphic/mylonitic S_1* schistosity in the juxtaposed Tobífera and Zapata thrust sheets. The fold hinges trend NW-SE and plunge from 30° to 70° to the northwest, asymmetry of fold limbs suggest a tectonic transport to the north.

At the eastern area of Canal Gajardo, mylonitic silicic metatuffs with metric intercalations of dark metapelitic rocks of the Tobífera Fm. (e.g. FC1749) constitute the hanging wall of the NW-SE-striking *Eastern Tobífera Thrust* (Figs. 2 and 3 A2). The S_1* foliation is subparallel to the sedimentary bedding and dips ~ 20-40° to the southwest. NE-trending stretching lineations with asymmetric sigma-shaped porphyroclasts contained in the volcano-sedimentary interface indicate a shear sense to the northeast (Table 1).

At Isla Escarpada in Seno Skyring (Fig. 2) the N-S trending eastern flank of the Escarpada Syncline exposes a thick succession of clast-supported conglomerates and conglomeratic sandstones of the Escarpada Fm. Where studied, the strata dip between 50° and 65° to the west.

tric intercalations of shales and greywackes are mapped as part of the *Sarmiento Ophiolitic Complex* (Figs. 2 and 3 B1). The mafic volcaniclastic rocks are variably folded showing steep stratification.

At the central area of Canal Jerónimo the pre-Jurassic metamorphic basement rocks crop-out in the hanging wall between two thrust sheets of the Tobífera Fm. (Figs. 2 and 3 B1). The NW-SE-striking S_1 schistosity in metapelitic schists is tightly folded (of ~ 30 cm wavelength) with subvertical axial planes defining the S_2 crenulation cleavage. This cleavage strikes NW-SE and dips from 20 to 65° generally to the southwest, but with some limbs dipping to the northeast, parallel to the thrust zone juxtaposing it onto the Tobífera Fm. (Fig. 3 B1).

At the northern area of Canal Jerónimo (Isla Santa María) silicic metatuffs of the Tobífera Fm. (e.g. FC1723) preserve the volcaniclastic bedding subparallel to the S_1* mylonitic cleavage, striking NNW-SSE and dipping ~ 80° to the west (Figs. 2 and 3 B1). A group of NNE-SSW-striking 1-10 cm thick quartz veins and tension gashes cut obliquely the mylonitic planes (S_1*), present echelon geometries and monoclinal cm-sized folds with sinistral east-vergence. Brittle normal faults, which have resulted in ~ 1-3 cm displacements of quartz veins and the S_1* cleavage, strike to the NNW-SSE and dip ~ 35° to the east.

At the southern area of Estero Wickham folded successions of silicic metatuffs with intercalations of shale-rich siliciclastic rocks of the Tobífera Fm. (e.g. FC1727 and FC1728) are internally folded and imbricated (Fig. 4). A ~ 20 m wavelength anticline of these successions is in the hanging wall of a NW-SE-striking thrust zone dipping ~ 40° to the west (Fig. 4 A). The NNW-SSE-striking axial plane is nearly subvertical. A brittle-ductile NW-SE-striking mylonitic S-C-type cleavage (S_1*) dips 30-60° to the southwest, and is oblique to the volcano-sedimentary bedding (Figs. 3 B1 and 4). In the footwall, the shale-rich beds bear 15 cm- thick layers of sandstones, which are boudinaged and dip ~ 30° to the southwest (Fig. 4 D). The S_1* mylonitic cleavage is oblique to the sedimentary bedding, strikes NW-SE and dips ~ 40° to the southwest. Further east, the Tobífera Fm. is thrust upon the Zapata Fm. through the *Eastern Tobífera Thrust* and dips ~ 35° to the southwest (Figs. 2 and 3 B1).

At the northern area of Estero Wickham the hundred-meter thick successions of siltstones belonging to the Canal Bertrand Fm. (Figs. 2 and 3 B2) are backthrusted onto the Zapata Fm. The sedimentary bedding (S_0) in Canal Bertrand Fm. strikes WNW-ESE and dips ~ 20-30° to the north and to the south. Siltstones show a NW-SE-trending cleavage, dipping ~ 10° to the southwest and northeast, in which few granitic lithic grains up to 0.7 cm in size are rotated and show shear sense indicators to the northeast (Table 1). Variations in the dip direction of S_0 and the cleavage reveal open folds of tens of meters wavelength.

1.15 4.2. Microstructures

1.15.14.2.1. Pre-Jurassic basement rocks

In metapsammopelitic schists at Canal Gajardo the S_1 foliation is defined by discontinuous up to 1 cm thick, discontinuous microlithons, mainly composed of up to 100 µm-sized polycrystalline quartz, and discontinuous mm-thick cleavage domains of up to 100 µm wide crystals of white mica with minor proportions of chlorite and opaques. The S_1 foliation is crenulated into up to 1 cm asymmetric tight folds with a 1 mm- spaced axial planar S_2 crenulation cleavage, defined by irregular planes of opaques. S_2 planes cross-cut perpendicularly the S_1 foliation causing reverse displacements of S_1 fold limbs to the north, interpreted as shear-sense indicators accordingly to meso-scale structures. The S_2 foliation is oblique and subparallel to the S_1* foliation observed in metatuffs and metasedimentary rocks of RVB, suggesting a common deformational event in the pre-Jurassic basement and the RVB units.

Metapelitic schists at Estero Wickham are composed of up to 100 µm-sized quartz, white mica, chlorite, opaque minerals and accessory apatite. Anastomosed cleavage domains constituted mainly of white mica present two oblique preferential planes, suggesting a S-C-type mylonitic foliation with shear sense to the northeast (Fig. 5 A, Table 1). Sigmoidal microlithons of polygonal quartz show undulose extinction and subgrains with core-mantle texture, which are indicators of dynamic recrystallization.

Remnants of ophiolitic rocks at the central area of Canal Gajardo correspond to greenish pillow basalts composed of up to 100 µm-sized tremolite-actinolite, plagioclase, chlorite, epidote, white mica, and titanite; carbonate is restricted to inter-pillow domains. Foliated metabasalts in the westernmost ophiolitic slice at Canal Gajardo contain up to 2 mm-sized porphyroblasts of actinolite and matrix consisting of up to 500 µm-sized plagioclase, chlorite, actinolite, titanite, epidote, quartz, carbonate, and traces of opaques. Cleavage domains (~ 100-300 µm thick) composed of preferentially orientated mats of chlorite and actinolite define the S_1* foliation; these domains are discontinuous with sigmoidal geometry, suggesting a shear sense to the northeast (Fig. 5 B). Asymmetrically deformed porphyroblasts of actinolite indicate a shear sense to the north (Table 1). The S_1* foliation is crenulated into disharmonic open mm-folds with an incipient axial planar S_2* foliation, and cross-cut by up to 1 mm thick veins of carbonate.

1.15.34.2.3. Tobífera Fm.

Mylonitic silicic metatuffs at Canal Gajardo (e.g. FC1749) bear up to 1 mm-sized porphyroclasts (15-20%) of quartz and minor plagioclase; sigma-shaped quartz porphyroclasts show asymmetric strain shadows of quartz, white mica, and opaques (Fig. 5 C); plagioclase is commonly fractured and exhibits trails of fluid inclusions truncated by cleavage domains of white mica and chlorite. Cleavage domains are anastomosed and define the mylonitic S_1* foliation with shear sense indicators to the northeast (Fig. 5 C; Table 1). The matrix is composed of up to 100 µm-sized quartz, feldspars, white mica, chlorite, and opaques. The dark metapelitic rocks intercalated within metatuffs bear up to 700 µm-sized porphyroclasts of microcrystalline quartz and subhedral opaques surrounded by asymmetric strain fringes of quartz, and fragmented by domino-type structures suggesting shear sense to the northeast (Fig. 5 D). The matrix is composed of preferred-oriented platy quartz, clay minerals and opaque crystals smaller than 100 µm defining the S_1* mylonitic cleavage.

Mylonitic silicic metatuffs at Canal Jerónimo (e.g. FC1723) bear mm-to-cm-sized porphyroclasts (<5%) of quartz, feldspar, and rhyolitic lithics lacking intracrystalline deformation, surrounded by asymmetric strain shadows of quartz with flakes of white mica. The recrystallized matrix is composed of up to 100 µm-sized quartz, white mica, chlorite, plagioclase, and non-oriented radial zoisite. Preferred orientation of mica in two oblique planes suggests an S-C-type mylonitic cleavage (S_1*) with shear sense to the northeast (Table 1). Late brittle structures such as quartz tension-gashes, show dextral and sinistral shear-sense indicators. At Canal Jerónimo a sedimentary breccia belonging to the Tobífera Fm. is constituted of mm-to-cm-sized rectangular clasts of polydeformed schist in a quartzose recrystallized matrix.

Mylonitic silicic metatuffs at Estero Wickham (e.g. FC1727) consist of up to 1 mm-sized and sigma-shaped porphyroclasts (5%) of quartz, alkali feldspar and plagioclase, which are internally fractured; their rims are truncated by cleavage domains of preferred-oriented micaceous and opaque minerals, formed through pressure-solution processes. Two oblique preferential planes define a S-C-type mylonitic cleavage (S_1*) with shear-sense indicators to the northeast (Fig. 4 B-C; Table 1). The matrix is dynamically recrystallized and composed of aggregates of up to 100 µm-sized quartz and feldspar, and preferred-oriented flakes of white mica and chlorite, opaques, and traces of titanite. The intercalated shale-rich metapelitic rocks bear sigma-shaped micron-sized grains of quartz, surrounded by anastomosed domains of preferred-oriented white mica, plagioclase, and accessory epidote, chlorite and opaques, defining a S_1* mylonitic cleavage (Fig. 4 E). Early quartz veins are crenulated and disrupted by cleavage domains of S_1*. Late quartz veins are undeformed and crosscut S_1*.

1.15.44.2.4. Zapata Fm.

Mylonitic metapsammopelites at Canal Gajardo (e.g. FC1754) are composed of 1-2 mm-thick microlithons of up to 500 µm-sized microcrystalline quartz with polygonal contacts, and anastomosed 0.5-1 mm-thick cleavage domains of up to 100 µm-sized crystals of white mica, chlorite, epidote, and opaques defining the S_1* foliation. This is crenulated into 1-to-10 mm wavelength open folds, with an axial planar S_2* crenulation cleavage defined by opaque-rich discontinuous layers. The rocks affected by contact

mica, plagioclase, quartz, epidote, and chlorite with no preferential orientation overprinting a relict fabric of S_1* (Fig. 5 E-F). The domains with relict S_1* foliation are 0.5 mm-wide bands with up to 300 µm-sized preferred oriented quartz with bulging and subgrain rotation, indicating dynamic recrystallization, with disharmonic folds of 1 mm wavelength (Fig. 5 E).

Metapsammopelitic rocks at the westernmost thrust sheet of Canal Gajardo are composed of up to 100 µm-sized quartz, white mica, opaques, and traces of chlorite and epidote. The preferred orientation of micas define the S_1* foliation that is crenulated; opaque-rich cleavage domains define an axial planar foliation S_2*. Mylonitic metapelites (e.g. SHP141) show a foliation defined by cleavage domains composed of up to 500 µm-long and 100 µm-wide aggregates of white mica, and chlorite smaller than 100 µm; and up to 100 µm-thick microlithons of quartz, albite, and traces of epidote and actinolite smaller than 100 µm.

1.15.54.2.5. Satellite plutons of the South Patagonian Batholith

The *Western Domain* of the MFTB is intruded by different igneous bodies (plutons and dykes) of quartz-diorite (e.g. FC1759), composed of up to 1 cm-sized crystals of subhedral plagioclase, uralitized clinopyroxene and variably chloritized hornblende, and up to 500 µm-sized interstitial quartz, and traces of subhedral magmatic titanite and opaques. Sample FC1759 was collected from an undeformed part of the pluton there the unit does not exhibit recrystallization textures.

1.15.64.2.6. Upper Cretaceous Units of the Magallanes-Austral Basin

The fine-grained siltstones of Canal Bertrand Fm. are composed of mm-sized detrital plagioclase and quartz in a matrix of up to 100 µm-sized clay minerals, white mica, chlorite, and opaques, cemented by carbonate. A cleavage defined by preferred orientation of chlorite, white mica, and opaque minerals is oblique to the sedimentary bedding. Rotated mm-to-cm-sized granite clasts in coarse-grained rocks show asymmetric strain shadows of micaceous and opaque minerals, indicating a sense of shear to the northeast (Table 1).

Clast-supported conglomerates of the Escarpada Fm. show imbricated well-rounded up to 10 cm-sized clasts of low sphericity. The main lithotypes of the clasts are shales, foliated rhyolites, aphanitic and porphyritic igneous rocks, and metasedimentary rocks. The matrix is composed of crystals of white mica, clay minerals and carbonates smaller than 10 µm. The compositional diversity of clasts is akin to those lithologies observed in the *Western Domain* of the MFTB, and thus considered here as a potential sediment source to submarine conglomerates deposited during the Late Cretaceous phase of sedimentation in the Magallanes-Austral Basin (cf. McAtamney et al., 2011). Further provenance analysis and stratigraphic study of these units is necessary to confirm this correlation.

1.16 4.3. Geochronology

1.16.14.3.1. Zircon U-Pb Geochronology

The zircon grains from the mylonitic silicic metatuff of the *Eastern Tobífera Thrust* (FC1727) predominantly show oscillatory zoning, indicating igneous crystallization, although many grains also have darker cathodoluminescent (CL) cores (higher U; Fig. 6 A). As the aim of this study was to determine the zircon crystallization age, 22 analyses were made on the brighter CL outer areas and whole grains, with only 4 darker CL cores analyzed (Table 2 A; Fig. 6 A). The dominant age grouping is at ca. 160 Ma with a subordinate tail at ca. 168 Ma and two other scattered Lower Jurassic and Upper Triassic analyses (Table 2 A; Fig. 6 A). Importantly, the calculated radiogenic $^{206}Pb/^{238}U$ ages do not vary significantly between rim and core in few analyzed grains. Analysis of one diffuse core records the presence of an older Triassic age (Table 2 A; Fig. 6 A). In terms of the dominant age grouping for analyses of the oscillatory zoned zircon, a weighted mean $^{206}Pb/^{238}U$ age for 21 analyses gives 159.9 ± 1.1 Ma (MSWD=1.4).

For the mylonitic metapsammopelite of the Zapata Fm. (FC1754), a random sampling of the total zircon fraction was poured onto double sided tape and prepared for detrital zircon analyses. The zircons range from euhedral prisms with bipyramidal terminations to sub-rounded/rounded grains; the CL images

range in detrital ages with significant Early Cretaceous, Permian, and Ordovician groupings (Fig. 6 B). The predominant Early Cretaceous grouping, comprising 28 analyses, can be arbitrarily unmixed in three groups (Fig. 6 C): there is a more prominent subgroup at ca. 130 Ma (n=14); a lesser sub-grouping around 125 Ma (n=12) and a minor cluster near 135 Ma (n=2). Minor components of Devonian, early Cambrian, Neoproterozoic, Mesoproterozoic and Archean ages are recorded in 12 analyzed grains (Table 2 B, Fig. 6 B). The scattered dates of 15 grains, ranging between 250 Ma and 290 Ma, suggest the presence of a Permian cluster near ca. 280 Ma. There are minor scattered clusters at ca. 410 Ma (n=4), ca. 470 Ma (n=8), and ca. 540 Ma (n=3).

Only five zircon grains were recovered from the heavy mineral concentrate for the hornblende quartz-diorite at Canal Gajardo (FC1759). All 5 grains show zoned igneous CL internal structures and record upper Cretaceous $^{206}Pb/^{238}U$ ages around 84-80 Ma (Fig. 6 D). Excluding a high U analysis with the youngest $^{206}Pb/^{238}U$ age, the weighted mean is 83.2 ± 1.0 Ma (MSWD = 0.45; Table 2 C, Fig. 6 D).

1.16.24.3.2. $^{40}Ar/^{39}Ar$ geochronology

Mats of white mica from the mylonitic metapelite of the Zapata Fm. (SHP141) from the western Canal Gajardo (Fig. 7 A) were dated *in situ* using an IR laserprobe for $^{40}Ar/^{39}Ar$ analyses. Representative major-element compositions of the analyzed white mica crystals (see Table 5) indicate their phengite composition with Si a.p.f.u. (atoms per formula unit) > 3.3, as shown in the classification diagram of Fig. 8 A, and Mg# = $Mg^{+2}/(Mg^{+2}+Fe^{+2})$ between 0.7 and 0.85. In chlorite Mg# is ~ 0.6.

Ten of eleven analysis spots (Table 3) on mats of ~ 100 µm-sized phengite yielded a weighted mean of 71.1 ± 1 Ma (MSWD = 5.9). The asymmetric distribution of data and MSWD higher than 1 (Fig 7 B) suggest more than one population within the dataset. The five youngest dates form a consistent group with a mean age of 70.2 ± 0.4 Ma; six dates can be grouped in an interval between 71 and 73 Ma, and one significantly older 75.5 ± 1.6 Ma date was excluded from the analysis due to its high error.

1.17 4.4. P-T Constraints

The P-T pseudosection modeling of four samples was used to constrain the depth of tectonic burial and temperature during the development of mylonitic bands in the hanging wall of the *Eastern Tobífera Thrust* and in the westernmost part of the MFTB. The metatuff samples were chosen because they present a well-preserved mylonitic foliation defined by metamorphic minerals that allow to constrain the P-T conditions of dynamic recrystallization. The metapsammopelite sample was chosen because it exhibits a hornfels texture defined by biotite, white mica, chlorite, and plagioclase, caused by contact metamorphism overprinting the S_1* foliation with dynamic recrystallization microstructures in quartz. This sample is located near the quartz-diorite pluton that was dated, allowing thus the relative dating of the different tectonic events in the *Western Domain* of the MFTB. To construct the P-T pseudosections we used the bulk-rock major-element composition (Table 4) and the mineral chemistry (Table 5) of these samples.

1.17.14.4.1. Petrography and mineral composition

Representative chemical compositions of white mica, chlorite, feldspar, biotite, and epidote of the analyzed samples are presented in Table 5. Classification diagrams for white mica (Ernst, 1963), chlorite (Foster, 1962) and feldspar (Deer et al., 1963) are shown in Figure 8 A-C, respectively. To characterize feldspar, we used the molar fraction $X_{Na} = Na^{+}/(Na^{+}+Ca^{+2}+K^{+})$. Epidote is characterized by the $Fe^{+3}/(Al+Fe^{+3})$ ratio = XFe^{3+}. Approximated modal compositions of analyzed samples are listed in Table 6 with the calculated compositions obtained from the P-T pseudosection modeling.

The silicic metatuff of the Tobífera Fm. at Canal Gajardo (FC1749) consists of quartz (~ 55%; including 15% of porphyroclasts), plagioclase (~ 25%; including 5% of porphyroclasts), white mica (15%), chlorite (5%) and traces of opaques. The Si and Al contents of phengitic white mica vary between 3.20 and 3.60 a.p.f.u. and 2.05 and 2.30 a.p.f.u., respectively (Fig. 8 A). The 5 µm-sized laths of chlorite (mostly absent in the mineral assemblage) have Si content of 3.13 a.p.f.u. and X_{Mg} of 0.8, and can be classified as

d
recrystallized matrix are albite in composition (X_{Na} of 0.95- 0.99; Fig. 8 C).

The mylonitic metapsammopelite of the Zapata Fm. at Canal Gajardo (FC1757) is composed by quartz (55%), plagioclase (25%), white mica (10%), biotite (5%), chlorite (4%), epidote (1%) and traces of opaques. Biotite is characterized by Mg# varying between 0.41 and 0.44. White mica shows Si and Al contents ranging between 3.12 and 3.30 a.p.f.u. and 2.15 and 2.60 a.p.f.u., respectively (Fig. 8 A). Chlorite is classified as ripidiolite with X_{Mg} of ~ 0.50 and Si contents around 2.78 a.p.f.u. (Fig. 8 B). Plagioclase is oligoclase with X_{Na} varying between 0.69 and 0.73 (Fig. 8 C).

The mylonitic silicic metatuff at Canal Jerónimo (FC1723) is composed of quartz (~ 55%; including 5% of porphyroclasts), white mica (30%), chlorite (10%), plagioclase (4%), epidote (1%) and traces of opaques. The phengitic composition of white mica is characterized by Si and Al contents varying between 3.10 and 3.30 a.p.f.u. and 2.35 and 2.60 a.p.f.u., respectively (Fig. 8 A). Two main groups of chlorite compositions were identified and correspond to clinochlore (Si = ~ 2.9 a.p.f.u.; X_{Mg} = ~ 0.8) and ripidiolite (Si = ~ 2.6 a.p.f.u.; X_{Mg} = ~ 0.4) (Fig. 8 B). Few grains show high X_{Mg} (~ 0.8) and higher Si content (>3.1 a.p.f.u.) (Fig. 8 B). Albite composition (X_{Na} of 0.95- 0.99; Fig. 8 C) was determined in porphyroclasts and within the quartz-rich recrystallized matrix. Epidote is classified as clinozoisite (*sensu* Seki, 1959), with XFe^{3+} = 0.10-0.12.

The mylonitic silicic metatuff at Estero Wickham (FC1727) consists of quartz (~ 50%; including 5% of porphyroclasts), plagioclase (25%), K-feldspar (5%), white mica (15%), chlorite (5%) and traces of opaques. The white mica is phengite, with Si and Al contents varying between 3.30 and 3.45 a.p.f.u. and 1.9 and 2.1 a.p.f.u., respectively (Fig. 8 A). Chlorite is classified as ripidolite with X_{Mg} between 0.40-0.44 and low Si contents (~ 2.8 a.p.f.u.; Fig. 8 B). Plagioclase is albite in composition (Fig. 8 C).

1.17.24.4.2. P-T Pseudosection Modeling

In the four selected samples the thermodynamic modeling was achieved in the TiMNCKMFASHO (TiO_2–MnO–Na_2O–CaO–K_2O–FeO–MgO–Al_2O_3–SiO_2–H_2O–O_2) system, within the range of pressures between 2 and 7 kbar and temperatures between 150 and 550°C. Bulk-rock compositions are presented in Tables 4 A (raw data) and 4 B (with corrections and normalization). The O_2 content is related to 10% of the iron to be trivalent suggested by the presence of magnetite in the rock. CaO was corrected due to presence of apatite. The percentage of oxides was normalized to 100% (Table 4 B). The H_2O content of each sample was based on the loss on ignition from the XRF analysis, with a maximum 4 wt% to guarantee a free hydrous fluid phase in the P-T pseudosection.

For the mylonitic silicic metatuff at Canal Gajardo (FC1749) the isopleths for Si = 3.36 a.p.f.u. in white mica (average value) and #Mg = 0.75 in chlorite (average value) intersect at ~ 3-4 kbar and ~ 210-250°C (Fig. 9 A). This is consistent with X_{Na} > 0.95 in plagioclase, predicted to be stable at temperature above 190ºC. At 3.5 kbar and 230°C the calculated volume percent of the mineral assemblage is quartz (46%), plagioclase (27%), white mica (16%), chlorite (3%), stilpnomelane (1%), clinopyroxene (0.2%), titanite (0.1%), plus water (6.7%). No rutile was detected under the microscope, but a good correspondence exists for major phases. Stilpnomelane and clinopyroxene were also not identified under the microscope; these minerals may have been decomposed by weathering, but other reasons for the presence of these phases in the calculation result such as imperfect solid-solution models are possible as well.

In the P-T pseudosection for the metapsammopelite with textures of contact metamorphism belonging to the Zapata Fm. at Canal Gajardo (FC1757) the intersection of the isopleths for Si = 3.18 a.p.f.u. in phengitic white mica (average value), the X_{Na} of 0.70 in plagioclase (average value), and Mg# of 0.44 in biotite (average = 0.42) match at ~ 5-6 kbar and 430-460°C (Fig. 9 B). At 5.5 kbar and 440°C the calculated volume percent of the mineral assemblage is quartz (55%), feldspar (19.5%), white mica (7%), biotite (2%), chlorite (3%), epidote (5%), and titanite (0.5%) plus water (8%). The isopleths of Mg# in chlorite (average = 0.48) do not intersect this field, probably because chlorite is not in equilibrium with biotite, phengite and plagioclase. According to the diagram, chlorite with of Mg# = 0.48 occur between temperatures of 230-250°C and may be result of retrograde metamorphism. Magnetite may be present as opaque mineral.

ion of the isopleths for Si = 3.21 a.p.f.u. in phengite (average value), X_{Na} = 0.99 in plagioclase (average value), Mg# = 0.82 in chlorite (clinochlore, average value) match at ~ 5.3-6.3 kbar and 420-460°C (Fig. 9 C). At 6 kbar and 450°C the calculated mineral assemblage is: quartz (55%), white mica (31%), chlorite (10%), plagioclase (0.5%), clinopyroxene (0.5%), plus water (3%). The disappearance of trace amounts of predicted clinopyroxene could be related to thermal increase accompanied by rising albite and epidote modal contents. However, an imperfect thermodynamic solid-solution model for Na-bearing clinopyroxene or other factors (e.g., selected O_2 content) could also account for the appearance of low amounts of clinopyroxene in the calculation results.

In the P-T pseudosection calculated for mylonitic silicic metatuff FC1727 the intersections of the isopleths for Si = 3.36-3.45 a.p.f.u. in phengite (average = 3.38), and Mg# between 0.40 and 0.42 in chlorite (average = 0.40) occur in the range 3-4 kbar at 300-340°C (Fig. 9 D). In consideration of plagioclase being almost pure albite, these conditions probably refer to the metamorphic peak. The calculated mineral assemblage at 3.8 kbar and 330°C is quartz (42%), plagioclase (30%), alkali feldspar (7%), white mica (13%), chlorite (2%), clinopyroxene (0.4%), titanite (0.2%), plus water (5.4%). Clinopyroxene and titanite were not identified in the petrographic thin section, maybe due to weathering. A good correspondence exists for major phases.

1.18 5. Discussion

1.19 5.1. Episodic magmatism and paleogeography of the Lobas Verdes Basin

The timing of magmatism during the Late Jurassic evolution of the RVB sheds important light on along-strike development of the extensional marginal basin during its ca. 40-50 myr history in southern South America. Our new ca. 160 Ma U-Pb zircon age from the silicic metatuff at Estero Wickham (FC1727 of the Tobífera Fm., Fig. 2 and 6 A) constrains the maximum depositional age of precursor silicic tuffs of the Tobífera Fm. It brings the age of Tobífera explosive silicic volcanism to the early Late Jurassic (Oxfordian) at this latitude of the orogenic system (~ 53°30'S). At this time, the Patagonian continental block (linked to South America) must have had continental connection with the Kalahari Craton to the northeast and the East Antarctic Craton to the southwest (Fig. 10 A, Dalziel et al., 2013). Three older zircons of ca. 168 Ma and one of ca. 165 Ma (Fig. 6 A) likely reflect xenocrystic inheritance or reworking of zircons from different Jurassic volcano-sedimentary sources. The Upper Triassic date in the diffuse core of one zircon was either incorporated into the original rhyolitic magma by upper crustal assimilation processes, or included into the pyroclastic and/or volcanoclastic deposits, during erosion of pre-Jurassic basement complexes.

Near Canal Jerónimo (~ 53°S) the ca. 157 Ma crystallization age of gabbros belonging to the *South Patagonian Batholith* (Hervé et al., 2007a) – at that time representing the parautochthonous magmatic arc to the west of the RVB (Fig. 10 A) – suggest coeval bimodal magmatism between 160-155 Ma. Clearly younger silicic magmatism is reported in northern areas (~ 49°-52°S), with Tithonian-Berriasian U-Pb zircon ages from metatuffs and hypabyssal rhyolitic rocks of the Tobífera Fm. ranging between ca. 154 and 140 Ma (Pankhurst et al., 2000; Calderón et al., 2007; Malkowski et al., 2015a; Zerfass et al., 2017), and ca. 150 Ma bimodal igneous suites of the *Sarmiento Ophiolitic Complex* (~ 51°30'S; Calderón et al., 2007). In extra-Andean Patagonia, silicic volcanic and volcaniclastic rocks buried beneath the sedimentary in-fill of the Magallanes-Austral basin (~ 53°S) have been dated at ca. 176 Ma (Pankhurst et al., 2000). Farther south, coeval and slightly older metatuffs at Cordillera Darwin (~ 55°S, Fuegian Andes) range in age between ca. 168 and ca. 162 Ma (Hervé et al., 2010b; Klepeis et al., 2010).

In this context, our ca. 160 Ma age reveals older rift-related volcanic events to the south of the RVB, and an episodic character of silicic volcanism during continental rifting. This finding may indicate that silicic magmatism and basin accommodation for deposition of volcanic rocks was controlled by the pre-Jurassic lithosphere-scale structures within the continental basement. Furthermore, our chronological data agree with northward younging ages that support the south to north unzipping mode of the opening of the RVB (cf. Stern and De Wit, 2003; Malkowski et al., 2015a), at least for the Patagonian sector of the

in Larsen Harbor (South Georgia Island), constrained by U-Pb zircon in plagiogranites, yielded crystallization ages of ca. 150 Ma (Mukasa and Dalziel, 1996), similar to the northern Sarmiento Ophiolitic Complex (Calderón et al., 2007). The progressive widening of the RVB and development of mid-ocean-ridge type spreading centers was established in Tierra de Fuego even later, with the emplacement of the Tortuga Ophiolitic Complex between 130-120 Ma (Calderón et al., 2013). Therefore, the silicic magmatism within the RVB seems to have been episodic during the rift-related opening of the RVB controlled by inherited basement structures, and subsequent seafloor spreading in mid-ocean-ridge type centers to the south-west (Fig. 10 A). The opening of the RVB is partially coeval with the opening of the Weddell Sea and the massive extension between South America and Africa that starts at ca. 130 Ma (Dalziel et al., 2013, Poblete et al., 2016).

The youngest cluster of detrital zircon dates of the metapsammopelite at Canal Gajardo (FC1754; Zapata Fm.) indicates a maximum depositional age of ca. 125 Ma at these latitudes (~ 52°30'-53°S). This age is coherent with the Barremian-Albian (ca. 130-100 Ma) age interval of the sandy upper sections of the Zapata/Erezcano and Beauvoir/Yaghan formations (Fildani et al., 2003; Calderón et al., 2007; Fosdick et al., 2011; Barbeau Jr. et al., 2009; Klepeis et al., 2010; Hervé et al., 2010b; Malkowski et al., 2015b), in southern Patagonia and Tierra del Fuego, respectively. The dominant detrital zircon age clusters (ca. 130 ± 1 Ma and 124 ± 1 Ma) suggest their derivation from volcanic and plutonic rocks from the westernmost magmatic arc now exposed in the *South Patagonian Batholith* (Hervé et al., 2007a). The secondary Paleozoic and subordinate older zircon populations indicate recycling of the pre-Jurassic basement complexes, with similar pre-Jurassic detrital zircon age distribution to those of metamorphic complexes in southern Patagonia (Hervé et al., 2003, 2008). This correlation accounts for incipient exhumation of the basement complexes during continental lithospheric stretching (Fig. 10 A), which may have shed sediments to the depocenters of the RVB (Fildani et al., 2003; Calderón et al., 2007).

5.2. Mylonites from the *Western Domain* of the MFTB and the *Eastern Tobífera Thrust*: underthrusting of the RVB and craton-ward transfer of shortening

Retro-arc deformation across the MFTB is linked to closure and inversion of the RVB that transferred shortening from southwest to northeast, leading to orogenic widening and consolidation. However, few through-going tectonic structures associated with RVB closure have been correlated along this orogenic belt. The mylonitic rocks from the Tobífera and Zapata formations located in the hanging wall of the *Eastern Tobífera Thrust* (~ 52°-54°S; Figs. 2, and 3 A2 and B2) and from the *Canal de las Montañas Shear Zone* (~ 51°-52°S; Calderón et al., 2012, Fig. 1) share craton-ward sense of shearing, low-grade metamorphic conditions, and a Late Cretaceous age. Taken together, we thus interpret these shear zones as a single continuous structure that extends from 51°S to 54°S within Tobífera and Zapata lithotypes, formed during the tectonic burial of the RVB successions. The *Canal de las Montañas Shear Zone* represents the sole thrust of the tectonic emplacement of the *Sarmiento Ophiolitic Complex* over the continental margin (Calderón et al., 2012). Here, we suggest that the mylonitic zones on top of the *Eastern Tobífera Thrust* also have a relevant role in the progressive underthrusting of oceanic and continental crust of the RVB (Fig. 10 B).

A partitioned deformation is observed in the mylonites of the *Western Domain*, where more competent quartz-feldspathic metatuffs experienced brittle-ductile deformation whereas less competent mica-rich metapelites and metapsammopelites exhibit dominant ductile features (*sensu* Hirth and Tullis, 1994). The coexistence of brittle and ductile structures suggest deformation at intermediate depths (~ 10 – 20 km depth, according to Stipp et al., 2002; Fossen and Cavalcante, 2017). The pervasive S_1* foliation in these lithotypes is seemingly related to northeast-vergent simple shearing dominated by pressure-solution processes.

The westward increase in the magnitude of ductile deformation across the strike of the *Western Domain* of the MFTB is interpreted from mesoscopic and microscopic observations at Canal Gajardo, regardless of the lithology. At the innermost part of the *Western Domain* tight folding of the S_1* foliation occurred, and transposition zones developed through the axial planar S_2* foliation. The S_1* and S_2*

formations, mafic ophiolitic bodies, and the pre-Jurassic basement complexes (Figs. 2 and 3 A1). Enhanced ductile deformation can be due to a release of fluids from dehydrated protoliths (metasedimentary and metavolcanic rocks) through deep shear zones, which may form an underthrusting interface (Tullis et al., 1982, 1996; van Staal et al., 2001; Massonne and Willner, 2008; Roche et al., 2018). In addition, magmatic hydrothermal fluids and increasing temperature may be due to the emplacement of satellite plutons of the *South Patagonian Batholith*. Thus, the development of S_1* and S_2* must have occurred in deep shear zones with hot fluid circulation within the RVB succession being underthrusted westwards beneath the parautochthonous magmatic arc (Fig. 10 B).

A critical wedge geometry is proposed from mechanical models of fold-and-thrust belts (Davis et al., 1983; Dahlen, 1990) and previous hypotheses regarding the RVB closure (Nelson et al., 1980; Gealey et al., 1980; Kohn et al., 1995; Harambour, 2002; Hervé et al., 2007b; Calderón et al., 2009, 2012; Klepeis et al., 2010). In pre-Jurassic metasedimentary rocks the S_2 foliation is subparallel to the RVB S_1* foliation. The time of formation of the S_2 foliation in the pre-Jurassic basement is not clear, but the correlation with the ductile structures of the RVB suggest a common Andean deformational event, in which the pre-Jurassic basement was underthrusted together with the RVB successions.

The *Eastern Tobífera Thrust* delimitates the mylonitic zones of the *Western Domain* of the MFTB in the east, emplacing brittle-ductile sheared rocks from the RVB over the Zapata rocks that show no ductile deformation nor metamorphism (Figs. 2 and 3). The uplift of deep ductile structures of the MFTB is ascribed to out-of-sequence craton-vergent thrusting and trench-vergent backthrusting from the end of Late Cretaceous to the early Oligocene (Nelson et al., 1980; Kohn et al., 1995; Harambour, 2002; Kraemer, 2003; Hervé et al., 2007b; Calderón et al., 2009, 2012; Klepeis et al., 2010; Maloney et al., 2011; Fosdick et al., 2011; Betka et al., 2015). The origin of the *Eastern Tobífera Thrust* may be associated with this protracted deformational event of uplift of the MFTB, and represents an important surface of juxtaposition of the deeply deformed successions with shallowly deformed successions (Fig. 10 C). Cross-cutting structures between the first-generation structures, resulting from the phase of deep underthrusting of the RVB, and the second-generation structures, resulting from the uplift of the MFTB are locally found (Betka et al., 2015). Inherited structures from the rift phase in the basement are reactivated during thrusting and backthrusting (Fig. 10 C), allowing the transfer of deformation to the east onto the Upper Cretaceous foreland basin (Nelson et al., 1980; Harambour, 2002; Rabalini et al., 2008; Fosdick et al., 2011; Betka et al., 2015). The reactivation of inherited faults in the basement and imbrication of the basement slices in the *Western Domain* of the MFTB resulted in a thick-skinned deformation superimposed to an early thin-skinned deformation (*sensu* Lacombe and Bellahsen, 2016).

1.21 5.3. Timing and thermobarometric conditions during the closure of the Rocas Verdes Basin

The development of brittle-ductile and ductile mylonitic fabrics in tectonically buried supracrustal rocks is controlled by the local geothermal gradient, plate boundary conditions, and the lithology of buried rocks (Ernst, 1971, 1972; Miyashiro, 1973; Tullis et al., 1982; Maruyama et al., 1996; Hirth and Tullis, 1994; Stipp et al., 2002; Wakabayashi and Dilek, 2003; Massonne and Willner, 2008; Fossen and Cavalcante, 2017). The mylonitic metatuffs of the *Western Domain* present a phengite+chlorite+quartz+albite metamorphic assemblage forming the S_1* foliation, typical of low-temperature metamorphic belts (McNamara, 1965; Vidal and Parra, 2000; Massonne and Willner, 2008; Bucher and Grapes, 2011). Pseudosection modeling shows that the metatuff at Canal Gajardo (FC1749) experienced prehnite-pumpellyite-facies metamorphism (~ 3-4 kbar and 210-250ºC), whereas the metatuff at Estero Wickham (FC1727) was metamorphosed at greenschist-facies conditions (~ 3-4 kbar and 300-340°C). Higher P-T conditions of greenschist-facies metamorphism (~ 5.3-6.3 kbar and 420-460°C) compared with the other analyzed metatuffs were estimated for the metatuff at Canal Jeronimo (FC1723). These P-T conditions are similar to those derived for the metapsammopelite at Canal Gajardo (FC1757, ~ 5-6 kbar and 430-460°C) based on the compositions of non-oriented biotite, muscovite, and plagioclase that overprinted oriented and folded bands of dynamically recrystallized quartz. From this textural feature, we interpret the estimated P-T conditions as recording local contact metamorphism in the metapsammopelite.

metatuff of Canal Jeronimo was slightly affected by contact metamorphism as well, explaining the occurrence of randomly oriented epidote in the metatuff. Although contact metamorphism may have affected these rocks locally, systematic pressure increases with temperature suggest a geotherm of regional metamorphism through about 3.5 kbar and 280°C, and 5.5 kbar and 430°C.

P-T constraints broadly agree with those derived for rocks in the *Canal de las Montañas Shear Zone* (~ 250-400°C, 6-7 kbar; Hervé et al., 2007b; Calderón et al., 2012). Thus we associate these and the studied rocks with a ~ 400 km long mylonitic and metamorphic belt of the Patagonian sector of the MFTB. Assuming intermediate geothermal gradients (~ 20°C/km; Miyashiro, 1973; Maruyama et al., 1996; Zheng et al., 2016) these rocks reached crustal depths between 10-23 km (Fig. 10 B). The dehydration of volcanic and sedimentary successions at depths of ~ 20 km would have released fluids that circulated along major thrusts, thereby favoring the offscraping and imbrication of ophiolitic tectonic slices in the underthrusted crustal stack (Massonne and Willner, 2008). These units crop out at Canal Gajardo (Figs. 1 and 2 A).

The metapsammopelite belonging to the Zapata Fm. at Canal Gajardo is located near the ca. 83 Ma quartz diorite pluton (FC1754), which is hypothesized here as the source of local thermal perturbation. With this interpretation on the timing of the thermal perturbation, combined with the fact that both the dated quartz diorite and the metamorphic minerals in the metapsammopelite are undeformed, we use this age constraint as the minimum age of dynamic recrystallization of the foliated bands (at least S1*) at Canal Gajardo. Similarly, Santonian-Campanian crystallization ages of satellite plutons emplaced in the *Western Domain* of the MFTB to the north of the study area (ca. 85-80 Ma between 51-52°S) and in the Fuegian Andes (ca. 86 Ma between 54-55°S), were interpreted as the minimum age of RVB underthrusting (Klepeis et al., 2010; Calderón et al. 2012). However, some of the Late Cretaceous satellite plutons near the study region show anisotropic fabrics near pluton margins, indicating that crustal deformation proceeded during the magmatic arc construction (Hervé et al., 2007a; Klepeis et al., 2010; Fosdick et al., 2011; Betka et al., 2015). Deep shear zones may control the ascent of the back-arc plutons especially during the extensional phases after orogenic thickening (Laurent et al., 2015). In this context, the analyzed quartz-diorite was likely emplaced after (or possible during the late stages of) the phase of underthrusting of the RVB units (that generated the S_1* foliation). The absence of deformational fabrics observed within the quartz diorite sample suggests that deformation migrated to shallower crustal levels some time before 83 Ma, and/or that the deformed parts of the intrusion and imbricated units of RVB were eroded or obscured by cover. Finally, we note that the ca. 83 Ma age is coeval with a pronounced zircon U-Pb age peak (ca. 80-66) present in detrital zircon age spectra from the Cenozoic Magallanes-Austral Basin successions (Fosdick et al., 2020), thereby providing additional indirect evidence for this phase of Late Cretaceous arc magmatism.

The syntectonic phengite of a mylonitic metapelite from the western part of Canal Gajardo yields a cluster of $^{40}Ar/^{39}Ar$ dates at ca. 70 Ma, with an older single-grain ages as old as ca. 73 Ma. We note that the grain size of phengite (up to 100 μm) is too small for any chemical zoning of micas relating to different episodes of crystallization to be recognized. Additionally, this age variability also may have been caused by a combination of analytical uncertainty, deformation, grain boundary effects and geological variability in the micas. The mineral assemblage in the sample is phengite+chlorite+zoisite+albite, which is consistent with greenschist-facies conditions of regional metamorphism, in accordance with P-T constraints from mylonitic rocks of the *Western Domain* (of ~ 3-6 kbar and ~ 210-460°C). Under the assumption that Ar mobility is mainly linked to thermally controlled volume diffusion, the retention of radiogenic Ar depends on the crystal size and temperature of metamorphism (Warren et al., 2012). In 100 μm grains, the retention of radiogenic Ar at temperatures < 350°C (the average estimated regional temperature) over 2 mya is between 90-95%. However, at ~ 460°C (the maximum regional temperature), Ar retention would decrease to ~35% over the same time interval (Warren et al., 2012). A possible reheating event may therefore have caused partial resetting of the deformational age. However, the recorded age is considerably younger than the nearby intrusion (ca. 83 Ma), what also reinforces the fact that the analysed quartz-diorite sample is from the inner undeformed part of the pluton and that its external parts could be deformed.

Our preferred interpretation is that the 70 Ma phengite age records the timing of syntectonic mineral growth during deformation. This interpretation is consistent with Coniacian-Maastrichtian $^{40}Ar/^{39}Ar$ dates in

Complex, which have been interpreted as recording the timing of deformation (Kohn et al., 1995; Maloney et al., 2011). Ductile thrusting in this complex operated at deep structural levels (~35 km) between 90-70 Ma, while backthrusting was concentrated in the shallow structural levels during the same interval (Kohn et al., 1995; Klepeis et al., 2010; Maloney et al., 2011). We thus interpret the ca. 73-70 Ma $^{40}Ar/^{39}Ar$ dates as recording the timing of deformation during the protracted exhumation history of mylonite belts in both the southern Patagonian and Fuegian Andes, but without further data the meaning of the dates older than 71 Ma cannot be tested. Campanian-Maastrichtian dynamic recrystallization in shallow crustal depths is consistent with the phase of out-of-sequence thrusting and backthrusting occurring until the early Oligocene (Kohn et al., 1995; Kraemer, 2003; Klepeis et al., 2010; Maloney et al., 2011; Fosdick et al., 2011; Betka et al., 2015), associated with the formation of the *Eastern Tobífera Thrust*. This episode is related to the uplift and extrusion of the underthrusted crustal stack in the *Western Domain* of the MFTB (Fig. 10 C). In the paleogeographic context, the Weddell Sea was in a relatively quiet tectonic period until 60 Ma, the Antarctic Peninsula was separated from South America and the ophiolite-bearing South Georgia Island was displaced to the east of the Fuegian Andes (Fig. 10 B-C; Gee and Kent, 2007; Dalziel et al., 2013; Poblete et al., 2016).

Finally, the phases of deformation and metamorphism that occurred between the Santonian and Maastrichtian reflects different magnitudes of hinterland exhumation between the southern Patagonian and Fuegian Andes. Along-strike of the southern Patagonian Andes (51°-54°S), linking our study region with the *Canal de las Montañas Shear Zone*, the exhumation of low-grade metamorphic rocks, dynamically recrystallized at crustal depths ranging between ~ 10 and 23 km, begins between ca. 83-70 Ma. Contrastingly, in the Fuegian Andes (54°-56° S) the metasedimentary rocks of the *Cordillera Darwin Metamorphic Complex* – a unique culmination of Paleozoic to Lower Cretaceous sedimentary successions metamorphosed at upper amphibolite facies during the Cretaceous – indicate exhumation of deeply buried rocks formed at ~ 35 km depth before ca. 73 Ma (Kohn et al., 1993, 1995; Klepeis et al., 2010; Maloney et al., 2011). Thus, the thermobarometric constraints show that the tectonic underthrusting of the RVB successions before the Campanian due to arc-continent collision involved deep shear zones, which were uplifted during the Late Cretaceous and Paleogene with a higher magnitude in the Fuegian Andes.

1.22 6. Conclusions

New field data, microstructural analysis, thermobarometry, U-Pb and $^{40}Ar/^{39}Ar$ geochronology from the southern Patagonian Andes provide kinematic, P-T, and time constraints on the opening and closure of the RVB. Zircon U-Pb ages constrain the maximum depositional ages of episodic silicic volcanism at ca. 160 Ma, and the hemipelagic sedimentation to ca. 125 Ma. The geographical distribution of silicic volcanic rocks in sub-basins, controlled by the geometry of pre-Jurassic rifting structures within the continental basement, was followed by mafic magmatism in mid-ocean ridge-type spreading centers located to the west and southwest of the paleo-continental margin. New microstructural data and P-T metamorphic constraints of 3-6 kbar and ca. 210-460°C in mylonitic silicic volcanic and metapsammopelitic rocks of RVB are compatible with tectonic underthrusting of the RVB's oceanic and continental crust in a deep crustal stack. West- and southwest-ward shear zones recorded in at least one brittle-ductile foliation (S_1*) in the *Western Domain* of the MFTB suggests tectonic accretion during the RVB closure, indicating tectonic burial to 10-23 km depths beneath the edge of the parautochthonous magmatic arc. The mylonitic and metamorphic belt extending from the *Canal de las Montañas Shear Zone* to the study area (~ 50-54ºS) constitute a ~ 400 km long lithospheric-scale structure that accommodated east- and northeast-verging shearing beneath the underthrusted crustal stack. Deformation migrated from this structure to shallow crustal levels prior to ca. 83 Ma, when Campanian satellite intrusions of quartz diorite caused contact metamorphism in the foliated metavolcano-sedimentary rocks. Finally, the ca. 70-73 Ma $^{40}Ar/^{39}Ar$ syntectonic phengite ages suggest a phase of Campaninan-Maastrichtian out-of-sequence thrusting and backthrusting, culminating with uplift and exhumation of the *Western Domain* of the MFTB.

This work was funded by the Fondecyt Project Nº 1161818 in Chile and by LAMIR/UFPR/PETROBRAS Research Project Nº 2016/00141-1 in Brazil. Special thanks to Alison Halton (The Open University) by the ^{40}Ar-^{39}Ar data processing, Andrea Stevens Goddard (Indiana University), Fernanda Torres (Andrés Bello University) and Diego Rojo (Arturo Prat University) for their support during field work, and the crew of the Marypaz II that made possible the navigation through the Patagonian fjords. We also thank all LAMIR (Federal University of Paraná) team for their technical and intellectual support during this research. Salvador Harambour kindly provided field data and the sample SHP141. This study is also part of the project MIUR – Dipartimenti di Eccellenza 2018–2022, Department of Earth and Environmental Sciences, University of Milano-Bicocca. PS was supported by the Italian MIUR (Rita Levi Montalcini grant, DM 694-26/2017). We acknowledge outstanding revisions and suggestions by Valentin Laurent, an anonymous reviewer, and the editor Philippe Agard.

Credit Author Statement:
Veleda Astarte Paiva Muller: Conceptualization, Formal Analysis, Investigation, Data Curation, Writing, Visualization
Mauricio Calderón: Conceptualization, Formal Analysis, Investigation, Resources, Writing, Visualization, Supervision, Project Administration, Funding Acquisition
Julie Fosdick: Conceptualization, Investigation, Writing
Matias Ghiglione: Conceptualization, Investigation, Writing, Visualization
Leonardo Fadel Cury: Conceptualization, Resources, Supervision, Funding Acquisition
Hans-Joachim Massonne: Conceptualization, Methodology, Formal Analysis, Investigation, Resources, Writing
Christopher Mark Fanning: Conceptualization, Methodology, Formal Analysis, Investigation, Resources, Writing
Clare Warren: Conceptualization, Methodology, Formal Analysis, Investigation, Resources, Writing
Cristobal Ramírez de Arellano: Conceptualization, Investigation
Pietro Sternai: Conceptualization, Writing, Supervision

Declaration of interests

The authors declare that they have no known competing financial interests or personal relationships that could have appeared to influence the work reported in this paper.

1.24 References

Agard, P., Yamato, P., Jolivet, L., Burov, E. 2009. Exhumation of oceanic blueschists and eclogites in subduction zones: timing and mechanisms. Earth-Science Reviews, 92(1-2), 53-79. doi.org/10.1016/j.earscirev.2008.11.002

Allen, R.B. 1982. Geología de la Cordillera Sarmiento, Andes Patagónicos, entre los 51º00' y 52º15' Lat. S, Magallanes, Chile. Servicio Nacional de Geología y Minería, Boletín 38, 1-46.

Allmendinger, R.W., Ramos, V.A., Jordan, T.E., Palma, M., Isacks, B.L. 1983. Paleogeography and Andean structural geometry, northwest Argentina. Tectonics, 2(1), 1-16. doi.org/10.1029/TC002i001p00001

Alvarez-Marrón, J., McClay, K.R., Harambour, S., Rojas, L., Skarmeta, J. 1993. Geometry and evolution of the frontal part of the Magallanes foreland thrust and fold belt (Vicuna-Area), Tierra del Fuego, Southern Chile. American Association of Petroleum Geologist Bulletin, 77, 1904–1921. doi.org/10.1306/BDFF8F74-1718-11D7-8645000102C1865D

Andersen, D.J., Lindsley, D.H. 1988. Internally consistent solution models for Fe-Mg-Mn-Ti oxides; Fe-Ti oxides. American Mineralogist, 73(7-8), 714-726.

Angiboust, S., Cambeses, A., Hyppolito, T., Glodny, J., Monié, P., Calderón, M., Juliani, C. 2018. A 100-my-long window onto mass-flow processes in the Patagonian Mesozoic subduction zone (Diego de Almagro Island, Chile). Geological Society of America Bulletin, 130(9-10), 1439-1456. doi.org/10.1130/B31891.1

Angiboust, S., Hyppolito, T., Glodny, J., Cambeses, A., Garcia-Casco, A., Calderón, M., Juliani, C. 2017. Hot subduction in the middle Jurassic and partial melting of oceanic crust in Chilean Patagonia. Gondwana Research, 42, 104-125. Doi.org/10.1016/j.gr.2016.10.007

Anguita, N.G. 2010. Petrogénesis de diques lamprofídicos postectónicos y su relación con el magmatismo shoshonítico Cretácico de la Formación Barros Arana y el Complejo La Pera, Magallanes, XII Región, Chile. Undergraduate Thesis, Universidad de Chile, Santiago, 237 p. (unpublished)

geochronology of the eastern Magallanes foreland basin: Implications for Eocene kinematics of the northern Scotia Arc and Drake Passage. Earth and Planetary Science Letters, 284(3-4), 489-503. doi.org/10.1016/j.epsl.2009.05.014

Bernhardt, A., Jobe, Z.R., Lowe, D.R. 2011. Stratigraphic evolution of a submarine channel-lobe complex system in a narrow fairway within the Magallanes foreland basin, Cerro Toro Formation, southern Chile. Marine and Petroleum Geology, 28(3), 785-806. doi.org/10.1016/j.marpetgeo.2010.05.013

Betka, P., Klepeis, K., Mosher, S. 2015. Along-strike variation in crustal shortening and kinematic evolution of the base of a retroarc fold-and-thrust belt: Magallanes, Chile 53°S–54°S. Geological Society of America Bulletin, 127 (7–8), 1108-1134. doi.org/10.1130/B31130.1

Betka, P.M. 2013. Structure of the Patagonian fold-thrust belt in the Magallanes region of Chile, 53°-55° S Lat. PhD Thesis, The University of Texas at Austin, 224 p. https://repositories.lib.utexas.edu/handle/2152/23239

Black, L.P., Kamo, S.L., Allen, C.M., Aleinikoff, J.N., Davis, D.W., Korsch, R.J., Foudoulis, C. 2003. TEMORA 1: a new zircon standard for Phanerozoic U–Pb geochronology. Chemical Geology, 200, 155-170. doi.org/10.1016/S0009-2541(03)00165-7

Braz, C., Seton, M., Flament, N., Müller, R.D. 2018. Geodynamic reconstruction of an accreted Cretaceous back-arc basin in the Northern Andes. Journal of Geodynamics, 121, 115-132.

Bruhn, R.L., Stern, C.R., de Wit, M.J. 1978. Field and geochemical data bearing on the development of a Mesozoic volcano-tectonic rift zone and back-arc basin in southernmost South America. Earth and Planetary Science Letters, 41(1), 32-46. doi.org/10.1016/0012-821X(78)90039-0

Bucher, K., Grapes, R. 2011. Petrogenesis of metamorphic rocks. Springer Science & Business Media.

Calderón, M., Fildani, A., Hervé, F., Fanning, C.M. 2007. Late Jurassic bimodal magmatism in the northern sea-floor remnant of the Rocas Verdes Basin, southern Patagonian Andes. Journal of the Geological Society of London, 164, 1011-1022. doi.org/10.1144/0016-76492006-102

Calderón, M., Fosdick, J., Alvarez, J., Sanchez, A., Galaz, G. 2009. Doubly-vergent structures in metamorphic rocks that enclose the Sarmiento Ophiolite Complex at Senos Lolos and Encuentros, Southern Patagonian Andes (51-52°S). XII Congreso Geológico Chileno, Santiago.

Calderón, M., Fosdick, J.C., Warren, C., Massonne, H.-J., Fanning, C.M., Fildani, A., Valley, J.W., Kitajima, K., Spicuzza, M.J., Fanning, C.M., Valley, L.F., Schwanethal, J., Fonseca, P.E., Galaz, G., Gaytán, D., Hervé, F. 2012. The low-grade Canal de las Montañas Shear Zone and its role in the tectonic emplacement of the Sarmiento Ophiolitic Complex and Late Cretaceous Patagonian Andes orogeny, Chile. Tectonophysics, 524, 165-185. doi.org/10.1016/j.tecto.2011.12.034

Calderón, M., Prades, C. F., Hervé, F., Avendaño, V., Fanning, C. M., Massonne, H.-J., Theye, T., Simonetti, A. 2013. Petrological vestiges of the Late Jurassic-Early Cretaceous transition from rift to back-arc basin in southernmost Chile: New age and geochemical data from the Capitán Aracena, Carlos III, and Tortuga ophiolitic complexes. Geochemical Journal, 47(2), 201-217. doi.org/10.2343/geochemj.2.0235

Castelli, J.C., Robertson, R., Harambour, A. 1992. Evaluación Geológica y Petrolera, bloques Ultima Esperanza Sur e Isla Riesco. Informe Archivo Técnico ENAP, Santiago, 59 p. (unpublished).

Charrier, R., Lahsen, A. 1969. Stratigraphy of Late Cretaceous-Early Eocene, Seno Skyring--Strait of Magellan Area, Magallanes Province, Chile. AAPG Bulletin, 53(3), 562-590. doi.org/10.1306/5D25C69D-16C1-11D7-8645000102C1865D

Connolly, J.A.D. 1990. Multivariable phase diagrams; an algorithm based on generalized thermodynamics. American Journal of Science, 290(6), 666-718. doi.org/10.2475/ajs.290.6.666

Cortés, R. 1964. Estratigrafía y un estudio de paleocorrientes del flysch Cretáceo del Depto. de Ultima Esperanza: Santiago, Chile. Undergraduate Thesis, Universidad Técnica de Estado, 117 p. (unpublished)

Coward, M.P. 1983. Thrust tectonics, thin skinned or thick skinned, and the continuation of thrusts to deep in the crust. Journal of Structural Geology, 5(2), 113-123. doi.org/10.1016/0191-8141(83)90037-8

Cox, K.G. 1992. Karoo igneous activity, and the early stages of breakup of Gondwanaland. In Magmatism and the causes of continental breakup (Storey, B.C.; Alabaster, T.; Pankhurst, R.J.; editors). Geological Society, Special Publications 68: 137-148.

Cunningham, W.D. 1995. Orogenesis at the southern tip of the Americas: the structural evolution of the Cordillera Darwin metamorphic complex, southernmost Chile. Tectonophysics, 244, 197-229. doi.org/10.1016/0040-1951(94)00248-8

Cunningham, W.D., Klepeis, K.A., Gose, W.A., Dalziel, I.W. 1991. The Patagonian Orocline: New paleomagnetic data from the Andean magmatic arc in Tierra del Fuego, Chile. Journal of Geophysical Research: Solid Earth, 96(B10), 16061-16067.

Dahlen, F. A. 1990. Critical taper model of fold-and-thrust belts and accretionary wedges. Annual Review of Earth and Planetary Sciences, 18(1), 55-99.

Dalziel, I.W., De Wit, M.J., Palmer, K.F. 1974. Fossil marginal basin in the southern Andes. Nature, 250, 291-294.

Dalziel, I.W., Lawver, L.A., Norton, I.O., Gahagan, L.M. 2013. The Scotia Arc: genesis, evolution, global significance. Annual Review of Earth and Planetary Sciences, 41.

Dalziel, I.W.D. 1981. Back-arc extension in the southern Andes: A review and critical reappraisal. Royal Society of London Philosophical Transactions A, 300, 319-335. doi.org/10.1098/rsta.1981.0067

Dalziel, I.W.D. 1986. Collision and Cordilleran orogenesis: an Andean perspective. In: Coward, M.P., Ries, A.C. (Eds.), Collision Tectonics. Geological Society of London Special publications, 19, 389-404. doi.org/10.1144/GSL.SP.1986.019.01.22

Davis, D., Suppe, J., Dahlen, F.A. 1983. Mechanics of fold-and-thrust belts and accretionary wedges. Journal of Geophysical Research: Solid Earth, 88(B2), 1153-1172. doi.org/10.1029/JB088iB02p01153

Deer, W.A., Rowie, R.A., Zussman, J. 1963. Rock Forming Minerals. 1st ed., vol. 4, London, Longman.

D 2647. doi.org/10.1029/JB075i014p0262
Eagles, G. 2016. Plate kinematics of the Rocas Verdes Basin and Patagonian orocline. Gondwana Research, 37, 98-109.
Ernst, W.G. 1963. Significance of phengitic micas from low-grade schists. American Mineralogist: Journal of Earth and Planetary Materials, 48(11-12), 1357-1373.
Ernst, W.G. 1971. Metamorphic zonations on presumably subducted lithospheric plates from Japan, California and the Alps. Contributions to Mineralogy and Petrology, 34(1), 43-59.
Ernst, W.G. 1972. Occurrence and mineralogic evolution of blueschist belts with time. American Journal of Science, 272(7), 657-668. doi.org/10.2475/ajs.272.7.657
Ernst, W.G. 2005. Alpine and Pacific styles of Phanerozoic mountain building: subduction-zone petrogenesis of continental crust. Terra Nova, 17(2), 165-188. doi.org/10.1111/j.1365-3121.2005.00604.x
Fildani, A., Cope, T.D., Graham, S.A., Wooden, J.L. 2003. Initiation of the Magallanes foreland basin: Timing of the southernmost Patagonian Andes orogeny revised by detrital zircon provenance analysis. Geology, 31, 1081-1084. doi.org/10.1130/G20016.1
Fildani, A., Hessler, A.M. 2005. Stratigraphic record across a retroarc basin inversion: Rocas Verdes-Magallanes Basin, Patagonian Andes, Chile. Geological Society of America Bulletin, 117, 1596-1614. doi.org/10.1130/B25708.1
Forsythe, R., Allen, R.B. 1980. The basement rocks of Península Staines, Región XII, Province of Última Esperanza, Chile. Revista Geológica de Chile, 10, 3-15. doi.org/10.5027/andgeoV7n2-a01
Fosdick, J.C., Graham, S.A., Hilley, G.E. 2014. Influence of attenuated lithosphere and sediment loading on flexure of the deep-water Magallanes retroarc foreland basin, Southern Andes: Tectonics, 33, 12, 2505-2525. Doi:10.1002/2014TC003684.
Fosdick, J.C., Grove, M., Hourigan, J.K., Calderon, M. 2013. Retroarc deformation and exhumation near the end of the Andes, southern Patagonia. Earth and Planetary Science Letters, 361, 504-517. doi.org/10.1016/j.epsl.2012.12.007
Fosdick, J.C., Romans, B.W., Fildani, A., Bernhardt, A., Calderón, M., Graham, S.A. 2011. Kinematic evolution of the Patagonian retroarc fold-and-thrust belt and Magallanes foreland basin, Chile and Argentina, 51°30's. Geological Society of America Bulletin 123, 1679-1698. doi.org/10.1130/B30242.1
Fosdick, J.C., VanderLeest, R.A., Bostelmann, E.J., Leonard, J.S., Peralta, R.U., Griffin, M., Oyarzún, J.L. 2019. Revised timing of Cenozoic Atlantic incursions and changing hinterland sediment sources during southern Patagonian orogenesis. Lithosphere. Doi.org/10.31223/osf.io/vqkds
Fosdick, J.C., VanderLeest, R.V., Bostelmann, J.E., Leonard, J.S., Ogalde, R., Oyarzún, J.L., and Griffin, M. 2020. Revised timing of Cenozoic Atlantic incursions and changing hinterland sediment sources during southern Patagonian orogenesis, Lithosphere. doi.org/10.2113/2020/8883099.
Fossen, H., Cavalcante, G. C. G. 2017. Shear zones–A review. Earth-Science Reviews, 171, 434-455.
Foster, M.D. 1962. Interpretation and a classification of the chlorite. US Geological Survey Professional Paper, 414, 1-33.
Fuenzalida, R., Covacevich, V. 1988. Volcanismo y bioestratigrafía del Jurásico y Cretácico Inferior en la Cordillera Patagónica, Región de Magallanes, Chile. In: V Congreso Geologico Chileno 3, H159-H183.
Fuhrman, M.L., Lindsley, D.H. 1988. Ternary-feldspar modeling and thermometry. American Mineralogist, 73(3-4), 201-215.
Gealey, W.K. 1980. Ophiolite obduction mechanism. In: Panayiotou, A. (Ed.), Ophiolites. Proceedings International Ophiolite Symposium, Cyprus. Cyprus Geological Survey, Nicosia, 228-243.
Gee, J.S., Kent, D.V. 2007. Source of oceanic magnetic anomalies and the geomagnetic polarity time scale. doi.org/10.7916/D8DV1V8P
Ghiglione, M.C., Naipauer, M., Sue, C., Barberón, V., Valencia, V., Aguirre-Urreta, B., Ramos, V.A. 2015. U-Pb zircon ages from the northern Austral basin and their correlation with the Early Cretaceous exhumation and volcanism of Patagonia. Cretaceous Research, 55, 116-128. doi.org/10.1016/j.cretres.2015.02.006
Ghiglione, M.C., Suarez, F., Ambrosio, A., Da Poian, G., Cristallini, E.O., Pizzio, M.F., Reinoso, R.M. 2009. Structure and evolution of the Austral Basin fold-thrust belt, southern Patagonian Andes. Revista de la Asociación Geológica Argentina, 65(1), 215-226.
Harambour, S. 1998. Structural evolution of the Magallanes Block, Magallanes (Austral) Basin, offshore Argentina, South Atlantic. MSc thesis, Royal Holloway, University of London, Royal Holloway New College, 136 p. (unpublished)
Harambour, S. 2002. Deep seated thrusts in the frontal part of the Magallanes fold and thrust belt, Ultima Esperanza, Chile. XV Congreso Geológico Argentino, 3. El Calafate, Argentina, p. 230. CD ROM.
Hervé, F., Calderón, M., Fanning, C.M., Kraus, S., and Pankhurst, R.J. 2010a. SHRIMP chronology of the Magallanes Basin basement, Tierra del Fuego: Cambrian plutonism and Permian high-grade metamorphism. Andean Geology, 37(2), 253-275. ISSN: 0718-7092
Hervé, F., Calderón, M., Faúndez, V. 2008. The metamorphic complexes of the Patagonian and Fuegian Andes. Geological Acta, 6, 43-53. ISSN: 1695-6133
Hervé, F., Fanning, C.M. 2003. Early Cretaceous subduction of continental crust at the Diego de Almagro archipelago, southern Chile. Episodes, 26, 285-289.
Hervé, F., Fanning, C.M., Pankhurst, R.J. 2003. Detrital zircon age patterns and provenance of the metamorphic complexes of southern Chile. Journal of South America Earth Sciences, 16, 107-123. doi.org/10.1016/S0895-9811(03)00022-1
Hervé, F., Fanning, C.M., Pankhurst, R.J., Mpodozis, C., Klepeis, K., Calderón, M., Thomson, S.N. 2010b. Detrital zircon SHRIMP U–Pb age study of the Cordillera Darwin Metamorphic Complex of Tierra del Fuego: sedimentary sources and

doi.org/10.1144/0016-76492009-124
Hervé, F., Massonne, H.-J., Calderón, M., Theye, T. 2007b. Metamorphic P-T conditions of Late Jurassic rhyolites in the Magallanes fold and thrust belt, Patagonian Andes, Chile. Journal of Iberian Geology 33, 5-16. ISSN: 1886-7995.
Hervé, F., Pankhurst, R.J., Fanning, C.M., Calderón, M., Yaxley, G.M. 2007a. The South Patagonian batholith: 150 my of granite magmatism on a plate margin. Lithos 97, 373-394. doi.org/10.1016/j.lithos.2007.01.007
Hervé, M., Suárez, M., Puig, A. 1984. The Patagonian Batholith S of Tierra del Fuego, Chile: timing and tectonic implications. Journal of the Geological Society, 141(5), 909-917. doi.org/10.1144/gsjgs.141.5.0909
Hirth, G., Tullis, J. 1994. The brittle-plastic transition in experimentally deformed quartz aggregates. Journal of Geophysical Research: Solid Earth, 99(B6), 11731-11747. doi.org/10.1029/93JB02873
Holland, T., Baker, J., Powell, R. 1998. Mixing properties and activity-composition relationships of chlorites in the system MgO-FeO-Al_2O_3-SiO_2-H_2O. European Journal of Mineralogy, 395-406. doi.org/10.1127/ejm/10/3/0395
Holland, T.J.B., Powell, R. 1998. An internally consistent thermodynamic data set for phases of petrological interest. Journal of Metamorphic Geology 16, 309-343. doi.org/10.1111/j.1525-1314.1998.00140.x
Horton, B.K. 2018. Tectonic regimes of the central and southern Andes: Responses to variations in plate coupling during subduction. Tectonics, 37(2), 402-429. doi.org/10.1002/2017TC004624
Hyppolito, T., Angiboust, S., Juliani, C., Glodny, J., Garcia-Casco, A., Calderon, M., Chopin, C. 2016. Eclogite-, amphibolite- and blueschist-facies rocks from Diego de Almagro Island (Patagonia): Episodic accretion and thermal evolution of the Chilean subduction interface during the Cretaceous. Lithos, 264, 422-440. doi.org/10.1016/j.lithos.2016.09.001
Jamieson, R.A., Beaumont, C., Fullsack, P., Lee, B. 1998. Barrovian regional metamorphism: Where's the heat?. Geological Society, London, Special Publications, 138(1), 23-51. doi.org/10.1144/GSL.SP.1996.138.01.03
Jolivet, L., Trotet, F., Monié, P., Vidal, O., Goffé, B., Labrousse, L., Agard, P. 2010. Along-strike variations of P–T conditions in accretionary wedges and syn-orogenic extension, the HP–LT Phyllite–Quartzite Nappe in Crete and the Peloponnese. Tectonophysics, 480(1-4), 133-148. doi.org/10.1016/j.tecto.2009.10.022
Katz, H.R. 1964. Some new concepts on geosynclinal development and mountain building at the southern end of South America. 22nd International Geological Congress, India, Proceedings, New Delhi, 4, 242-255.
Klepeis, K., Betka, P., Clarke, G., Fanning, M., Hervé, F., Rojas, L., Mpodozis, C., Thomson, S.N. 2010. Continental underthrusting and obduction during the Cretaceous closure of the Rocas Verdes rift basin, Cordillera Darwin, Patagonian Andes. Tectonics, 29(3), TC3014. doi:10.1029/2009TC002610.
Kley, J., Monaldi, C.R., Salfity, J.A. 1999. Along-strike segmentation of the Andean foreland: causes and consequences. Tectonophysics, 301(1-2), 75-94. doi.org/10.1016/S0040-1951(98)90223-2
Kohn, M.J., Spear, F.S., Dalziel, I.D. 1993. Metamorphic P-T paths from Cordillera Darwin, a core complex in Tierra del Fuego, Chile: Journal of Petrology, 34, 519-542. doi.org/10.1093/petrology /34 .3 .519.
Kohn, M.J., Spear, F.S., Harrison, T.M., Dalziel, I.W.D. 1995. 40Ar/39Ar geochronology and P-T-t paths from the Cordillera Darwin metamorphic complex, Tierra del Fuego, Chile. Journal of Metamorphic Geology, 13(2), 251-270. doi.org/10.1111/j.1525-1314.1995.tb00217.x
Kraemer, P.E. 1998. Structure of the Patagonian Andes: Regional balanced cross section at 50 S, Argentina. International Geology Review, 40(10), 896-915. doi.org/10.1080/00206819809465244
Kraemer, P.E. 2003. Orogenic shortening and the origin of the Patagonian orocline (56 S. Lat). Journal of South American Earth Sciences, 15(7), 731-748.
Lacombe, O., Bellahsen, N. 2016. Thick-skinned tectonics and basement-involved fold–thrust belts: insights from selected Cenozoic orogens. Geological Magazine, 153(5-6), 763-810. doi.org/10.1017/S0016756816000078
Laurent, V., Beaudoin, A., Jolivet, L., Arbaret, L., Augier, R., Rabillard, A., Menant, A. 2015. Interrelations between extensional shear zones and synkinematic intrusions: The example of Ikaria Island (NE Cyclades, Greece), Tectonophysics, 651, 152-171. ISSN: 0040-1951
Lee, J.Y., Marti, K., Severinghaus, J.P., Kawamura, K., Yoo, H.S., Lee, J.B., Kim, J.S. 2006. A redetermination of the isotopic abundances of atmospheric Ar. Geochimica et Cosmochimica Acta, 70(17), 4507-4512.
Likerman, J., Burlando, J.F., Cristallini, E.O., Ghiglione, M.C. 2013. Along-strike structural variations in the Southern Patagonian Andes: insights from physical modeling. Tectonophysics, 590, 106-120. doi.org/10.1016/j.tecto.2013.01.018
Ludwig, K.R. 2000. SQUID 1.00, A User's Manual. Berkeley Geochronology Center Special Publication, 2, 2455.
Malkowski, M.A., Grove, M., Graham, S.A. 2015a. Unzipping the Patagonian Andes—Long-lived influence of rifting history on foreland basin evolution. Lithosphere, 8(1), 23-28. doi.org/10.1130/L489.1
Malkowski, M.A., Sharman, G.R., Graham, S.A., Fildani, A. 2015b. Characterization and diachronous initiation of coarse clastic deposition in the Magallanes–Austral retroarc foreland basin, Patagonian Andes. Basin Research, 29, 298-326. doi.org/10.1111/bre.12150
Maloney, K.T., Clarke, G.L., Klepeis, K.A., Fanning, C.M., and Wang, W. 2011. Crustal growth during back-arc closure: Cretaceous exhumation history of Cordillera Darwin, southern Patagonia. Journal of Metamorphic Geology, 29(6), 649-672. doi: 10 .1111 /j.1525-1314 .2011 .00934 .x
Maruyama, S., Liou, J.G., Terabayashi, M. 1996. Blueschists and eclogites of the world and their exhumation. International Geology Review, 38(6), 485-594. doi.org/10.1080/00206819709465347
Massonne, H.-J. 2010. Phase relations and dehydration behaviour of calcareous sediments at very-low to low grade metamorphic conditions. Periodico di Mineralogia, 79(2), 21-43.

in a subduction channel. Journal of Petrology, 53, 1969-1998. doi.org/10.1093/petrology/egs040
Massonne, H.-J., Willner, A. 2008. Phase relations and dehydration behaviour of psammopelites and mid-ocean ridge basalt at very-low to low grade metamorphic conditions. European Journal of Mineralogy 20, 867-879. doi.org/10.1127/0935-1221/2008/0020-1871
McAtamney, J., Klepeis, K., Mehrtens, C., Thomson, S., Betka, P., Rojas, L., Snyder, S. 2011. Along-strike variability of back-arc basin collapse and the initiation of sedimentation in the Magallanes foreland basin, southernmost Andes (53–54.5°S). Tectonics, 30 (5), TC5001. doi.org/10.1029/2010TC002826
McNamara, M. 1965. The lower greenschist facies in the Scottish Highlands. Geologiska Föreningen i Stockholm Förhandlingar, 87(3), 347-389.
Miyashiro, A. 1973. Paired and unpaired metamorphic belts. Tectonophysics, 17(3), 241-254. doi.org/10.1016/0040-1951(73)90005-X
Mpodozis, C., Alvarez, P., Elgueta, S., Mella, P., Hervé, F., Fanning, M. 2007. Revised Cretaceous stratigraphy of the Magallanes foreland basin at Seno Skyring: Regional implications of new SHRIMP age data on detrital zircon populations. In GEOSUR 2007 International Congress on the Geology and Geophysics of the Southern Hemisphere: Santiago, Chile, Pontificia Universidad Católica de Chile, abstract, p. 106.
Mukasa, S.B., Dalziel, I.W. 1996. Southernmost Andes and South Georgia Island, North Scotia Ridge: zircon U-Pb and muscovite 40Ar39Ar age constraints on tectonic evolution of Southwestern Gondwanaland. Journal of South American Earth Sciences, 9(5-6), 349-365.
Nelson, E.P. 1982. Post-tectonic uplift of the Cordillera Darwin orogenic core complex: Evidence from fission track geochronology and closing temperaturetime relationship. Journal of the Geological Society, 139, 755-761. Doi.org/10.1144/gsjgs.139.6.0755
Nelson, E.P., Dalziel, I.W.D., Milnes, A.G. 1980. Structural geology of the Cordillera Darwin; collisional style orogenesis in the southernmost Chilean Andes. Eclogae Geologie Helvetica, 73(3), 727-751.
Pankhurst, R.J., Leat, P.T., Sruoga, P., Rapela, C.W., Márquez, M., Storey, B.C., Riley, T R. 1998. The Chon Aike province of Patagonia and related rocks in West Antarctica: a silicic large igneous province. Journal of Volcanology and Geothermal Research, 81(1-2), 113-136. doi.org/10.1016/S0377-0273(97)00070-X
Pankhurst, R.J., Riley, T.R., Fanning, C.M., Kelley, S.P. 2000. Episodic silicic volcanism in Patagonia and the Antarctic Peninsula: Chronology of magmatism associated with the break-up of Gondwana. Journal of Petrology, 41, 605-625. doi.org/10.1093/petrology/41.5.605
Pfiffner, O.A. 2006. Thick-skinned and thin-skinned styles of continental contraction. Special papers-Geological Society of America, 414, 153.
Platt, J.P. 1986. Dynamics of orogenic wedges and the uplift of high-pressure metamorphic rocks. Geological Society of America Bulletin, 97(9), 1037-1053. doi.org/10.1130/0016-7606(1986)97<1037:DOOWAT>2.0.CO;2
Poblete, F., Roperch, P., Arriagada, C., Ruffet, G., Ramírez de Arellano, C., Hervé, F., Poujol, M. 2016. Late Cretaceous–early Eocene counterclockwise rotation of the Fuegian Andes and evolution of the Patagonia–Antarctic Peninsula system. Tectonophysics, 668, 15-34.
Prades, C.F.K. 2008. Petrología y metamorfismo de las rocas basálticas en Isla Capitán Aracena, Isla Carlos III y Estero La Pera, Región de Magallanes, Chile. Undergraduate Thesis, Departamento de Geología, Universidad de Chile, 136 p. (unpublished) http://repositorio.uchile.cl/handle/2250/104950
Price, N.J., McClay, K.R. (Eds.). 1981. Thrust and nappe tectonics. Geological Society of London.
Ramos, V. 1999. Plate tectonic setting of the Andean Cordillera. Episodes, 22, 183-190. doi.org/10.18814/epiiugs/1999/v22i3/005
Ramos, V.A., Zapata, T., Cristallini, E., Introcaso, A. 2004. The Andean thrust system: latitudinal variations in structural styles and orogenic shortening. In: McClay, K. (ed.), Thrust Tectonics and Hydrocarbon Systems, American Association of Petroleum Geologists: Memoir, AAPG, Tulsa, 82, 30–50.
Rapalini, A.E., Calderón, M., Singer, S., Hervé, F., Cordani, U. 2008. Tectonic implications of a paleomagnetic study of the Sarmiento Ophiolitic Complex, southern Chile. Tectonophysics 452, 29-41. doi.org/10.1016/j.tecto.2008.01.005
Renne, P.R., Balco, G., Ludwig, K.R., Mundil, R., Min, K. 2011. Response to the comment by WH Schwarz et al. on "Joint determination of 40K decay constants and 40Ar∗/40K for the Fish Canyon sanidine standard, and improved accuracy for 40Ar/39Ar geochronology" by PR Renne et al.(2010). Geochimica et Cosmochimica Acta, 75(17), 5097-5100.
Renne, P.R., Swisher, C.C., Deino, A.L., Kramer, D.B., Owens, T.L., DePaolo, D.J. 1998. Intercalibration of standards, absolute ages and uncertainities in 40Ar/39Ar dating. Chemical Geology ,145, 117-152. doi.org/10.1016/S0009-2541(97)00159-9
Roche, V., Sternai, P., Guillou-Frottier, L., Menant, A., Jolivet, L., Bouchot, V., Gerya, T. 2018. Emplacement of metamorphic core complexes and associated geothermal systems controlled by slab dynamics. Earth and Planetary Science Letters, 498, 322-333. doi.org/10.1016/j.epsl.2018.06.043
Rojas, L., Mpodozis, C. 2006. Geología estructural de la Faja Plegada y Corrida del sector chileno de Tierra del Fuego, Andes patagónicos australes. In Congreso Geológico Chileno, No. 11: Actas (Vol. 1).
Romans, B.W., Fildani, A., Hubbard, S.M., Covault, J.A., Fosdick, J.C., Graham, S.A. 2011. Evolution of deep-water stratigraphic architecture, Magallanes Basin, Chile. Marine and Petroleum Geology, 28, 612-628. doi.org/10.1016/j.marpetgeo.2010.05.002
Schellart, W.P. 2008. Overriding plate shortening and extension above subduction zones: a parametric study to explain formation of the Andes Mountains. Geological Society of America Bulletin, 120, 1441-1454. doi.org/10.1130/B26360.1

in East Asia. Journal of the Geological Society, 162(6), 959-972.
Seki, Y. 1959. Relation between chemical composition and lattice constants of epidote. American Mineralogist: Journal of Earth and Planetary Materials, 44(7-8), 720-730.
Selzer, C., Buiter, S.J., Pfiffner, O.A. 2007. Sensitivity of shear zones in orogenic wedges to surface processes and strain softening. Tectonophysics, 437(1-4), 51-70. doi.org/10.1016/j.tecto.2007.02.020
SERNAGEOMIN, 2003. Mapa Geológico de Chile: digital version. Geological Base scale 1:1.000.000. Chile Government, Servicio Nacional de Geología y Minería.
Stern, C.R. 1979. Open and closed system igneous fractionation within two Chilean ophiolites and the tectonic implications. Contribution to Mineralogy and Petrology 68, 243-258.
Stern, C.R., De Wit, M.J. 2003. Rocas Verdes ophiolites, southernmost South America: remnants of progressive stages of development of oceanic-type crust in a continental margin back-arc basin. Geological Society of London, Special Publications, 218, 665-683. doi.org/10.1144/GSL.SP.2003.218.01.32
Stern, C.R., Mohseni, P.P., Fuenzalida, P.R. 1991. Petrochemistry and tectonic significance of Lower Cretaceous Barros Arana Formation basalts, southernmost Chilean Andes. Journal of South American Earth Sciences, 4(4), 331-342. doi.org/10.1016/0895-9811(91)90005-6
Stipp, M., Stünitz, H., Heilbron, M., Schmid, D.W. 2002. The eastern Tonale fault zone: a natural laboratory for crystal plastic deformation of quartz over a temperature range from 250 to 700 °C. Journal of Structural Geology, 24, 1861-1884. doi.org/10.1016/S0191-8141(02)00035-4
Suárez, M., Pettigrew, T.H. 1976. An upper Mesozoic island-arc–back-arc system in the southern Andes and South Georgia. Geological Magazine, 113(4), 305-328. doi.org/10.1017/S0016756800047592
Suárez, R., González, P.D., Ghiglione, M.C. 2019. A review on the tectonic evolution of the Paleozoic-Triassic basins from Patagonia: Record of protracted westward migration of the pre-Jurassic subduction zone. Journal of South American Earth Sciences, 102256. doi.org/10.1016/j.jsames.2019.102256
Tera, F., Wasserburg, G. 1972. U-Th-Pb systematics in three Apollo 14 basalts and the problem of initial Pb in lunar rocks. Earth and Planetary Science Letters 14, 281-304. doi.org/10.1016/0012-821X(72)90128-8
Thomson, S.N., Hervé, F., Stöckhert, B. 2001. Mesozoic-Cenozoic denudation history of the Patagonian Andes (southern Chile) and its correlation to different subduction processes. Tectonics, 20(5), 693-711. doi.org/10.1029/2001TC900013
Tullis, J., Snoke, A.W., Todd, V.R. 1982. Significance and petrogenesis of mylonitic rocks. Geology, 10, 227-230. doi.org/10.1130/0091-7613(1982)10<227:SAPOMR>2.0.CO;2
Tullis, J., Yund, R., Farver, J. 1996. Deformation-enhanced fluid distribution in feldspar aggregates and implications for ductile shear zones. Geology, 24(1), 63-66. doi.org/10.1130/0091-7613(1996)024<0063:DEFDIF>2.3.CO;2
van Staal, C.R., Rogers, N., Taylor, B.E. 2001. Formation of low-temperature mylonites and phyllonites by alkali-metasomatic weakening of felsic volcanic rocks during progressive, subduction-related deformation. Journal of Structural Geology, 23(6-7), 903-921. doi.org/10.1016/S0191-8141(00)00163-2
Vidal, O., Parra, T. 2000. Exhumation paths of high-pressure metapelites obtained from local equilibria for chlorite–phengite assemblages. Geological Journal, 35(3-4), 139-161. doi.org/10.1002/gj.856
Wakabayashi, J., Dilek, Y. 2003. What constitutes 'emplacement' of an ophiolite?: Mechanism and relationship to subduction initiation and formation of metamorphic soles. In: Dilek, Y., Robinson, P.T. (Eds.), Ophiolites in Earth History: Geological Society, London, Special Publications, 218, 427-447. doi.org/10.1144/GSL.SP.2003.218.01.22
Warren, C.J., Hanke, F., Kelley, S.P. 2012. When can muscovite 40Ar/39Ar dating constrain the timing of metamorphic exhumation?. Chemical Geology, 291, 79-86. doi.org/10.1016/j.chemgeo.2011.09.017
Williams, I.S. 1998. U-Th-Pb geochronology by ion microprobe. In: McKibben, M.A., Shanks III, W.C., Ridley, W.I. (Eds.), Applications of Microanalytical Techniques to Understanding Mineralizing Processes: Reviews in Economic Geology, 107, 1-35.
Willner, A.P., Hervé, F., Thomson, S.N., Massonne, H.-J. 2004. Converging PT-paths of Mesozoic HP-LT metamorphic units (Diego de Almagro Island, Southern Chile, 51°30pS): Evidence for juxtaposition during late shortening of an active continental margin. Mineralogy and Petrology, 81, 43-84.
Wilson, T.J. 1991. Transition from back-arc to foreland basin development in southernmost Andes: Stratigraphic record from the Ultima Esperanza District, Chile. Geological Society of America Bulletin, 103, 98-111. doi.org/10.1130/0016-7606(1991)103<0098:TFBATF>2.3.CO;2
Winslow, M.A. 1982. The structural evolution of the Magallanes Basin and neotectonics in the southernmost Andes. Antarctic Geoscience, 143-154.
Zerfass, H., Ramos, V.A., Ghiglione, M.C., Naipauer, M., Belotti, H.J., Carmo, I.O. 2017. Folding, thrusting and development of push-up structures during the Miocene tectonic inversion of the Austral Basin, Southern Patagonian Andes (50°S). Tectonophysics. 699, 102-120. doi.org/10.1016/j.tecto.2017.01.010
Zheng, Y., Chen, R., Xu, Z., Zhang, S. 2016. The transport of water in subduction zones. Science China Earth Sciences, 59(4), 651-682.

Table 1: List of *in situ* oriented samples showing the attitude of foliation corresponding to S_1* in RVB units, the thin section orientation, and the respective shear sense interpreted from asymmetric microtectonic and/or mesoscale structures. The attitudes are dip direction/dip angle.

Locality	Coordinates	Unit	Lithology	Sample	S_0	S_1*		Thin section		Plane	Shear sense
Canal Jerónimo	S53° 22.038' W72° 25.660'	pre-Jurassic basement	Metapelitic schist	FC1721		235	32	199	55	xz	NE
Isla Santa Cruz (Canal Jerónimo)	S53° 12.592' W72° 28.992'	Tobífera Fm.	Mylonitic metatuff	FC1723		265	85	309	31	yz	NE-sinistral
Estero Wickham	S53° 25.090' W72° 09.259'	Tobífera Fm.	Mylonitic metatuff	FC1727		230	25	89	90	xz	NE
Estero Wickham	S53° 23.663' W72° 07.333'	Tobífera Fm.	Metapsammite	FC1729		175	28	119	60	xz	NE
Estero Wickham	S53° 18.979' W72° 06.379'	Latorre Fm.	Slate	FC1731	170/9	10	22	189	75	xz	NE
Canal Gajardo (spot 1)	S52° 43.218' W72° 43.841'	Tobífera Fm.	Mylonitic metatuff	FC1739		230	25	296	80	xz	NE
Canal Gajardo (spot 3)	S52° 45.421' W72° 46.252'	pre-Jurassic basement	Metapsammopelitic schist	FC1753		230	49	158	90	xz	N
Canal Gajardo (spot 10)	S52° 51.004' W72° 58.737'	Sarmiento Ophiolite	Foliated metabasalt	FC1763		225	20	349	85	yz	N
Canal Gajardo (spot 10)	S52° 51.004' W72° 58.737'	Sarmiento Ophiolite	Foliated metabasalt	FC1765		25	45	159	80	yz	NE

Table 2 A: SHRIMP U-Pb results for zircon crystals within the silicic metatuff of the Tobífera Fm. (FC1727) at Estero Wickham.

							Total				Radiogenic			Age (Ma)
Grain. spot	U (ppm)	Th (ppm)	Th/U	^{206}Pb* (ppm)	$^{204}Pb/^{206}Pb$	f206 %	$^{238}U/^{206}Pb$	±	$^{207}Pb/^{206}Pb$	±	$^{206}Pb/^{238}U$	±	$^{206}Pb/^{238}U$	±
1.1	411	249	0.61	8.9	0.000336	0.14	39.80	0.48	0.0504	0.0011	0.0251	0.0003	159.8	1.9
2.1	299	133	0.45	6.5	-	0.35	39.55	0.49	0.0520	0.0012	0.0252	0.0003	160.4	2.0
2.2	3035	1556	0.51	66.1	0.000090	0.68	39.47	0.44	0.0547	0.0030	0.0252	0.0003	160.2	1.9
3.1	154	66	0.43	3.3	0.000270	<0.01	39.87	0.56	0.0489	0.0019	0.0251	0.0004	159.8	2.3
3.2	476	264	0.55	9.9	0.000107	0.01	41.28	0.50	0.0492	0.0009	0.0242	0.0003	154.3	1.9
4.1	426	239	0.56	9.4	-	0.31	39.06	0.46	0.0517	0.0010	0.0255	0.0003	162.5	1.9
4.2	1776	922	0.52	38.6	0.000027	0.07	39.49	0.41	0.0498	0.0004	0.0253	0.0003	161.1	1.7
5.1	2689	1582	0.59	60.8	0.000012	<0.01	37.97	0.39	0.0490	0.0004	0.0263	0.0003	167.7	1.7
6.1	3119	1607	0.52	70.3	0.000043	<0.01	38.11	0.39	0.0489	0.0003	0.0263	0.0003	167.1	1.7
7.1	571	388	0.68	12.3	0.000022	0.11	39.82	0.46	0.0502	0.0008	0.0251	0.0003	159.7	1.8
8.1	262	151	0.58	5.6	0.000478	0.34	40.48	0.51	0.0519	0.0013	0.0246	0.0003	156.8	2.0
8.2	1563	602	0.39	33.0	0.000072	0.03	40.64	0.43	0.0494	0.0005	0.0246	0.0003	156.7	1.7
9.1	332	212	0.64	7.1	-	<0.01	40.16	0.49	0.0492	0.0011	0.0249	0.0003	158.5	1.9
10.1	831	491	0.59	18.4	0.000155	0.34	38.89	0.42	0.0520	0.0007	0.0256	0.0003	163.1	1.8
10.2	2490	1368	0.55	54.8	0.000024	<0.01	39.02	0.41	0.0487	0.0004	0.0256	0.0003	163.3	1.7
11.1	237	133	0.56	5.1	0.000256	0.26	40.22	0.53	0.0513	0.0013	0.0248	0.0003	157.9	2.1

13.1	420	215	0.51	9.0	0.000180	0.15	40.03	0.50	0.0504	0.0010	0.0249	0.0003	158.8	2.0
14.1	457	250	0.55	9.8	0.000134	0.25	39.94	0.46	0.0513	0.0009	0.0250	0.0003	159.0	1.8
15.1	151	70	0.46	3.8	0.002035	1.08	33.64	0.52	0.0584	0.0020	0.0294	0.0005	186.8	2.9
16.1	190	83	0.44	4.1	0.000334	0.34	39.95	0.54	0.0520	0.0015	0.0249	0.0003	158.8	2.2
17.1	615	387	0.63	13.5	0.000130	<0.01	39.20	0.44	0.0493	0.0008	0.0255	0.0003	162.4	1.8
18.1	609	373	0.61	12.9	0.000156	<0.01	40.62	0.47	0.0482	0.0008	0.0246	0.0003	157.0	1.8
19.1	264	91	0.35	8.4	-	0.01	27.03	0.33	0.0510	0.0010	0.0370	0.0005	234.1	2.8
20.1	1250	1063	0.85	28.5	0.000022	0.03	37.70	0.40	0.0497	0.0005	0.0265	0.0003	168.7	1.8
21.1	628	463	0.74	13.6	0.000281	0.17	39.75	0.50	0.0506	0.0008	0.0251	0.0003	159.9	2.0
22.1	297	144	0.48	6.3	0.000257	0.17	40.40	0.51	0.0505	0.0012	0.0247	0.0003	157.4	2.0

Notes:
1. Uncertainties given at the 1σ level.
2. Error in Temora reference zircon calibration was 0.31% for the analytical session (not included in above errors but required when comparing data from different mounts).
3. f_{206} % denotes the percentage of ^{206}Pb that is common Pb.
4. Correction for common Pb for the U/Pb data has been made using the measured ^{238}U/^{206}Pb and ^{207}Pb/^{206}Pb ratios following Tera and Wasserburg (1972) as outlined in Williams (1998).

Table 2 B: SHRIMP U-Pb results for zircon crystals within a metapsammopelite of the Zapata Fm. (FC1754) at Canal Gajardo.

							Total Ratios						Radiogenic Ratios						Age (Ma)				
Grain. spot	U (ppm)	Th (ppm)	Th/U	^{206}Pb* (ppm)	^{204}Pb/^{206}Pb	f206 %	^{238}U/^{206}Pb	±	^{207}Pb/^{206}Pb	±	^{206}Pb/^{238}U	±	^{207}Pb/^{235}U	±	^{207}Pb/^{206}Pb	±	ρ	^{206}Pb/^{238}U	±	^{207}Pb/^{206}Pb	±	% Disc
1.1	568	76	0.13	79	0.000041	0.07	6.186	0.068	0.0755	0.0016	0.1615	0.0018	1.669	0.040	0.0749	0.0016	0.460	965	10	1066	43	9
2.1	773	596	0.77	14	0.000138	0.23	46.956	0.558	0.050	0.0009	0.0212	0.0003						136	2			
3.1	257	75	0.29	28	-	<0.01	7.902	0.096	0.0757	0.0008	0.1266	0.0015	1.321	0.022	0.0757	0.0008	0.740	768	9	1087	22	29
4.1	357	387	1.08	6	0.000457	0.36	49.655	0.676	0.0515	0.0014	0.0205	0.0003						131	2			
5.1	111	72	0.65	2	-	0.12	48.013	0.975	0.0496	0.0025	0.0205	0.0004						131	3			
6.1	207	75	0.36	15	-	0.01	11.495	0.146	0.0583	0.0009	0.0870	0.0011						538	7			
7.1	319	36	0.11	21	-	<0.01	13.196	0.161	0.0548	0.0008	0.0759	0.0009						472	6			
8.1	251	79	0.31	17	0.000042	<0.01	12.658	0.160	0.0564	0.0009	0.0791	0.0010						490	6			
9.1	348	120	0.34	14	0.000139	<0.01	21.841	0.271	0.0520	0.0009	0.0458	0.0006						289	4			
10.1	480	59	0.12	31	-	0.04	13.199	0.151	0.0568	0.0007	0.0757	0.0009						471	5			
11.1	300	326	1.08	130	0.000015	0.02	1.989	0.023	0.1861	0.0007	0.5027	0.0057	12.886	0.154	0.1859	0.0007	0.952	2625	25	2706	6	3
12.1	57	40	0.70	1	0.002984	2.15	51.867	1.424	0.0656	0.0036	0.0189	0.0005						120	3			
13.1	272	241	0.89	8	0.000415	0.04	29.215	0.394	0.0508	0.0012	0.0342	0.0005						217	3			
14.1	139	79	0.57	2	0.001976	0.23	48.675	0.865	0.0505	0.0021	0.0205	0.0004						131	2			
15.1	95	43	0.45	2	0.000831	0.69	50.506	1.051	0.0540	0.0028	0.0197	0.0004						126	3			
16.1	281	88	0.31	49	-	<0.01	4.928	0.058	0.0838	0.0007	0.2030	0.0024	2.354	0.033	0.0841	0.0007	0.828	1191	13	1295	16	8

1						1	7			1	9	6	5								
18.1	138	96	0.69	2	0.000783	<0.01	49.936	0.933	0.0453	0.0021	0.0201	0.0004						128	2		
19.1	114	57	0.50	2	-	0.33	48.319	0.947	0.0513	0.0025	0.0206	0.0004						132	3		
20.1	273	111	0.40	18	0.000107	0.07	13.335	0.166	0.0569	0.0009	0.0749	0.0010						466	6		
21.1	560	216	0.39	22	0.000030	0.24	21.577	0.251	0.0540	0.0008	0.0462	0.0005						291	3		
22.1	292	102	0.35	11	0.000172	0.02	22.738	0.293	0.0520	0.0011	0.0440	0.0006						277	4		
23.1	418	113	0.27	26	0.000043	0.06	13.708	0.159	0.0565	0.0007	0.0729	0.0009						454	5		
24.1	462	81	0.17	52	0.000011	0.02	7.625	0.087	0.0678	0.0006	0.1311	0.0015	1.223	0.018	0.0677	0.0006	0.769	794	8	858	20	7
25.1	429	94	0.22	24	-	0.10	15.304	0.179	0.0557	0.0007	0.0653	0.0008						408	5		
26.1	125	56	0.45	2	0.000568	0.16	49.166	0.918	0.0499	0.0023	0.0203	0.0004						130	2		
27.1	78	75	0.96	3	0.000313	<0.01	22.393	0.414	0.0514	0.0020	0.0447	0.0008						282	5		
28.1	67	36	0.53	3	0.000423	<0.01	23.000	0.444	0.0504	0.0022	0.0436	0.0008						275	5		
29.1	52	22	0.42	1	0.001169	0.30	51.146	1.381	0.0509	0.0039	0.0195	0.0005						124	3		
30.1	269	100	0.37	5	0.000921	0.15	47.963	0.709	0.0499	0.0015	0.0203	0.0003						133	2		
31.1	570	313	0.55	101	-	<0.01	4.850	0.053	0.0844	0.0004	0.2012	0.0022	2.402	0.031	0.0845	0.0006	0.856	1209	12	1303	13	7
32.1	55	29	0.53	1	-	0.13	53.278	1.428	0.0499	0.0037	0.0187	0.0005						120	3		
33.1	108	38	0.35	6	0.000390	0.40	14.735	0.222	0.0585	0.0018	0.0676	0.0010						422	6		
34.1	172	122	0.71	6	-	<0.01	23.342	0.738	0.0519	0.0014	0.0428	0.0006						270	4		
35.1	47	25	0.54	1	0.002269	10.69	46.656	1.205	0.1334	0.0069	0.0191	0.0006						122	4		
36.1	746	309	0.41	29	0.000041	<0.01	23.141	0.248	0.0515	0.0006	0.0452	0.0005						285	3		
37.1	90	39	0.43	1	0.000431	0.45	52.517	1.136	0.0520	0.0028	0.0190	0.0004						121	3		
38.1	122	52	0.43	2	0.000452	<0.01	50.652	0.972	0.0480	0.0023	0.0198	0.0004						126	2		
39.1	391	245	0.63	51	-	<0.01	6.596	0.074	0.0792	0.0006	0.1517	0.0017	1.667	0.024	0.0797	0.0007	0.797	911	10	1189	17	23
40.1	72	37	0.52	1	0.000004	0.19	46.566	1.056	0.0503	0.0030	0.0214	0.0005						137	3		
44.2	1692	29	0.02	95	0.000034	0.04	15.360	0.160	0.0552	0.0004	0.0651	0.0007						406	4		
41.1	929	778	0.84	34	0.000037	0.03	23.328	0.257	0.0519	0.0006	0.0429	0.0005						271	3		
42.1	77	48	0.62	3	0.000644	0.18	21.716	0.400	0.0535	0.0020	0.0460	0.0009						290	5		
43.1	81	30	0.37	6	-	<0.01	11.429	0.185	0.0577	0.0015	0.0876	0.0014						541	9		
44.1	193	42	0.22	22	-	<0.01	7.471	0.094	0.0739	0.0009	0.1338	0.0017	1.364	0.024	0.0739	0.0009	0.714	810	10	1038	25	22
45.1	749	356	0.47	28	0.000040	0.04	23.156	0.259	0.0520	0.0007	0.0432	0.0005						272	3		
46.1	128	62	0.48	2	0.000286	0.07	50.985	0.945	0.0491	0.0023	0.0196	0.0004						125	2		
47.1	169	109	0.64	3	0.000247	0.48	49.656	0.885	0.0524	0.0022	0.0200	0.0004						128	2		

4					6		6		6	6	0	7								
49.1	672	38	0.06	44	0.000017	0.04	13.238	0.145	0.0568	0.0005	0.0755	0.0008					469	5		
50.1	782	58	0.07	61	-	0.20	11.051	0.119	0.0604	0.0005	0.0903	0.0010					557	6		
51.1	695	159	0.23	45	-	<0.01	13.276	0.147	0.0559	0.0006	0.0754	0.0008					468	5		
52.1	242	160	0.66	4	0.000314	<0.01	51.601	0.793	0.0479	0.0017	0.0194	0.0003					124	2		
53.1	64	32	0.50	1	0.000710	0.05	51.977	1.306	0.0488	0.0033	0.0192	0.0005					123	3		
54.1	439	264	0.60	8	0.000364	<0.01	47.684	0.628	0.0478	0.0012	0.0210	0.0003					134	2		
55.1	609	501	0.82	21	-	0.09	25.214	0.290	0.0519	0.0008	0.0396	0.0005					251	3		
56.1	99	53	0.54	2	0.000184	0.60	51.418	1.043	0.0533	0.0027	0.0193	0.0004					123	3		
57.1	56	25	0.46	1	0.001789	0.09	49.985	1.326	0.0493	0.0035	0.0200	0.0005					128	3		
58.1	374	222	0.59	6	-	<0.01	52.133	0.718	0.0473	0.0013	0.0192	0.0003					123	2		
59.1	215	107	0.50	38	0.000084	0.14	4.805	0.059	0.0844	0.0008	0.2078	0.0025	2.684	0.039	0.0832	0.0009	0.737	1217	14	1274	22	4
60.1	226	86	0.38	43	0.000004	0.01	4.488	0.054	0.0874	0.0007	0.2228	0.0027	2.683	0.039	0.0874	0.0007	0.827	1297	14	1368	16	5
61.1	157	80	0.51	22	0.000040	0.07	6.082	0.078	0.0812	0.0009	0.1643	0.0021	1.827	0.033	0.0806	0.0010	0.710	981	12	1213	25	19
62.1	440	89	0.20	82	-	<0.01	4.588	0.051	0.0833	0.0006	0.2130	0.0024	2.510	0.033	0.0835	0.0006	0.849	1271	13	1281	13	1
63.1	463	224	0.48	31	-	0.10	12.878	0.147	0.0577	0.0007	0.0776	0.0009						482	5			
64.1	591	369	0.62	20	0.000070	<0.01	24.969	0.292	0.0513	0.0008	0.0401	0.0005						253	3			
65.1	132	64	0.49	2	0.000356	<0.01	50.719	0.929	0.0497	0.0022	0.0198	0.0004						126	2			
66.1	301	198	0.66	5	0.000355	0.16	52.215	0.757	0.0497	0.0015	0.0191	0.0003						122	2			
67.1	144	69	0.48	2	0.000513	0.04	50.052	0.906	0.0489	0.0022	0.0200	0.0004						127	2			
68.1	250	234	0.93	4	-	<0.01	49.160	0.740	0.0479	0.0016	0.0204	0.0003						130	2			
69.1	621	502	0.81	23	0.000158	<0.01	23.175	0.267	0.0513	0.0007	0.0432	0.0005						272	3			
70.1	970	459	0.47	56	0.000010	0.02	14.872	0.160	0.0553	0.0005	0.0672	0.0007						419	4			

Notes:
1. Uncertainties given at the 1σ level.
2. Error in Temora reference zircon calibration was 0.31% for the analytical session (not included in above errors but required when comparing data from different mounts).
3. f_{206} % denotes the percentage of ^{206}Pb that is common Pb.
4. For areas older than ca. 800 Ma correction for common Pb made using the measured $^{204}Pb/^{206}Pb$ ratio.
5. For areas younger than ca. 800 Ma correction for common Pb made using the measured $^{238}U/^{206}Pb$ and $^{207}Pb/^{206}Pb$ ratios following Tera and Wasserburg (1972) as outlined in Williams (1998).
6. For % Disc. 0% denotes a concordant analysis.

Table 2 C: SHRIMP U-Pb results for zircon crystals separated from a quartz-diorite satellite pluton of the *South Patagonian Batholith* (FC1759) intruding the RVB units at Canal Gajardo.

								Total		Radiogenic		Age (Ma)				
Grain.	U	Th	Th/U	$^{206}Pb*$	$^{204}Pb/$	f206	$^{238}U/$	$^{207}Pb/$	$^{206}Pb/$	$^{206}Pb/$						

1.1	452	353	0.78	5.1	0.000023	0.27	76.06	0.99	0.0498	0.0013	0.0131	0.0002	84.0	1.1
2.1	1459	1346	0.92	16.3	-	0.09	76.92	0.84	0.0484	0.0007	0.0130	0.0001	83.2	0.9
3.1	454	277	0.61	5.1	-	0.14	76.81	0.96	0.0488	0.0013	0.0130	0.0002	83.3	1.0
4.1	1840	1077	0.59	19.9	0.000113	0.02	79.33	0.85	0.0478	0.0006	0.0126	0.0001	80.7	0.9
5.1	293	177	0.60	3.2	-	0.15	77.85	1.07	0.0489	0.0016	0.0128	0.0002	82.2	1.1

Notes:
1. Uncertainties given at the 1σ level.
2. Error in Temora reference zircon calibration was 0.31% for the analytical session (not included in above errors but required when comparing data from different mounts).
3. f_{206} % denotes the percentage of ^{206}Pb that is common Pb.
4. Correction for common Pb for the U/Pb data has been made using the measured ^{238}U/^{206}Pb and ^{207}Pb/^{206}Pb ratios following Tera and Wasserburg (1972) as outlined in Williams (1998).

Table 3: ^{40}Ar/^{39}Ar data of the mylonitic metapelite of Zapata Fm. (SHP1411) at Canal Gajardo.

40Ar	+/-	39Ar	+/-	38Ar	+/-	37Ar	+/-	36Ar	+/-	40Ar*/ 39Ar	+/-	Age	+/-	+/- (no J error)	39/40	+/-	36/40	+/-	37/39	+/-	38/
285971.96	777.91	75407.84	140.34	2.74	2.27	5990.66	135.88	76.35	1.72	3.49	0.01	**7[illegible].6**	**0.4**	0.28	0.26	0	0	0	0.08	0	3.6E
285233.26	768.11	77111.30	130.32	1.09	1.90	5497.19	135.93	58.83	1.53	3.47	0.0[illegible]	**71.6**	**0.4**	0.26	0.27	0	0.	0	0.07	0	1.4E
365927.21	1810.14	100863.27	290.69	7.75	2.19	13219.52	135.98	69.45	1.81	3.42	0.[illegible]	**70.6**	**0.5**	0.42	0.28	0	0	0	0.13	0	7.7E
331500.75	1212.63	92878.29	210.51	5.66	1.97	5673.16	136.03	58.14	1.44	3.[illegible]	0.02	**69.8**	**0.5**	0.32	0.28	0	0	0	0.06	0	6.1E
227792.46	573.68	59978.87	110.28	3.88	1.83	2937.69	136.12	54.68	1.4[illegible]	[illegible]3	0.01	**72.7**	**0.4**	0.27	0.26	0	0	0	0.05	0	6.5E
367902.47	2209.53	101346.00	210.51	6.66	1.60	9301.34	136.16	51.9[illegible]	1.44	3.48	0.02	**71.7**	**0.6**	0.47	0.28	0	0	0	0.09	0	6.6E
51762.21	*288.73*	*7702.62*	*33.13*	*2.27*	*1.46*	*2603.01*	*136.21*	*78.8[illegible]*	*1.81*	*3.66*	*0.08*	***75.5***	***1.7***	*1.62*	0.15	0	0	0	0.34	0.02	2.9E
243961.90	886.03	63503.03	150.37	1.46	2.12	5401.96	136.25	[illegible]7.81	1.72	3.52	0.02	**72.6**	**0.5**	0.36	0.26	0	0	0	0.09	0	2.3E
895338.53	1631.85	256476.77	290.77	8.77	4.38	10441.22	304.0[illegible]	[illegible]4.02	1.61	3.40	0.01	**70.2**	**0.4**	0.15	0.29	0	0	0	0.04	0	3.4E
210864.66	377.74	57991.27	93.28	5.29	4.12	6743.26	3[illegible].16	[illegible].21	1.34	3.40	0.01	**70.1**	**0.4**	0.22	0.28	0	0	0	0.12	0.01	9.1E
162905.01	346.13	43676.13	78.25	4.02	4.09	3142.52	[illegible]4.25	48.46	1.43	3.40	0.01	**70.1**	**0.4**	0.28	0.27	0	0	0	0.07	0.01	9.2E

Corrections:
Atmospheric 40/36 correction 298.[illegible] (Lee et al., 2006)
40/36 discimination value 295
J value 0.[illegible]1546801 +/- 0.5%
calculated using standard GA1550, with an age of 99.738 +/- 0.104Ma, Renne et al. (2011)
Potassium correction applied: 0.0085 +/-4.25E-05
Calcium ^{36}Ar correction applied: 0.000265 +/-1.325E-06
Calcium ^{39}Ar correction applied: 0.00065 +/-3.25E-06
blank corrected using average of days blanks
Decay constant of Renne et al. (2011)
^{37}Ar and ^{39}Ar corrected for decay between irradiation and analysis
irradiation: 100MWH
Analysis:
Nu Instruments Noblesse
*Spot 7 is an outlier and was not used to calculate the mean age

Table 4: Major-element compositions of the mylonitic silicic metatuffs of Tobífera Fm. (FC1723, FC1727, FC1749) and the metapsammopelite of Zapata Fm. (FC1757): A) Original XRF data; B) Corrected and normalized to 100% data.

A	**FC1723**	**FC1727**	**FC1749**	**FC1757**	**B**	**FC1723**	**FC1727**	**FC1749**	**FC1757**
SiO_2	72.25	77.48	77.67	79.00	SiO_2	73.11	77.20	76.68	78.35
TiO_2	0.09	0.12	0.07	0.25	TiO_2	0.09	0.12	0.06	0.25

Fe_2O_3	1.68	1.52	1.05	2.06	FeO	1.53	1.36	0.93	1.84
MnO	0.01	0.03	0.03	0.03	O_2	0.01	0.01	0.01	0.01
MgO	3.69	0.61	1.54	0.75	MnO	0.01	0.03	0.03	0.03
CaO	0.26	0.08	0.06	1.90	MgO	3.73	0.61	1.52	0.75
Na_2O	0.65	3.68	3.63	2.42	CaO	0.26	0.08	0.06	1.80
K_2O	3.04	2.59	1.65	1.11	Na_2O	0.66	3.67	3.58	2.40
P_2O_5	0.00	0.00	0.00	0.07	K_2O	3.08	2.58	1.63	1.10
Sum	95.00	97.51	97.39	97.17	H_2O	4.05	2.99	3.95	3.97
					Sum	100	100	100	100

Corrections:
O_2 = FeO*0.05*0.1113 (relative to 10% of trivalent iron)
CaO=CaO-(290.4/212.92)*P2O5
H_2O based on loss on ignition of each sample
Normalized to 100%

Table 5: Representative electron microprobe analyses (in wt%) of phengitic white mica (pheng), chlorite (chl), biotite (bt), epidote (ep), and feldspar (fs) in metatuffs of Tobífera Fm. (FC1723, FC1727, FC1749), metapsammopelite (FC1727), and metapelite (SHP141) of Zapata Fm.

Sample	FC 1723	FC 1727	FC 1749	FC 1757	SHP 141		FC 1723	FC 1723	FC 1727	FC 1749	FC 1757		FC 1757		FC 1723		FC 1723	FC 1727	FC 1749	FC 1757
Mineral	pheng	pheng	pheng	pheng	pheng		chl	chl	chl	chl	chl		bt		ep		fs	fs	fs	fs
SiO_2	49.63	49.76	51.97	49.01	48.61	SiO_2	35.61	23.68	25.24	33.73	26.41	SiO_2	35.58	SiO_2	38.19	SiO_2	67.79	69.41	68.06	62.28
TiO_2	0.01	0.15	0.05	0.25	0.08	TiO_2	0	0.02	0.02	0.02	0.01	TiO_2	2.87	TiO_2	0.02	TiO_2	0	0	0	0.01
Al_2O_3	32.83	25.73	29.64	28.29	27.61	Al2O3	26.7	20.94	22.14	23.13	19.83	Al_2O_3	17.44	Al_2O_3	29.73	Al_2O_3	19.78	19.42	19.5	24.57
FeO	0.89	3.8	0.81	0.18	1.14	FeO	7.53	31.3	30.91	11.33	26.96	FeO	21.35	Cr_2O_3	0	Cr_2O_3	0	0	0	0
Fe_2O_3	0	1.29	0	4.89	1.83	MnO	0.04	0.36	0.77	0.36	0.58	Fe_2O_3	0	Fe_2O_3	5.68	Fe_2O_3	0.13	0	0.12	0.24
MnO	0	0.05	0	0.05	0.07	MgO	21.35	11.33	12.06	21.65	14.55	MnO	0.27	Mn_2O_3	0	Mn_2O_3	0	0	0	0
MgO	2.21	3.18	3.59	3.83	3.78	CaO	13.41	10.95	10.93	12.89	11.36	MgO	8.69	MgO	0.05	MgO	0	0	0.01	0
CaO	0.05	0.01	0.02	0.03	0.03	Total	104.64	98.58	98.34	103.12	99.71	CaO	0.02	CaO	24.25	CaO	0.28	0.12	0.11	5.74
Na_2O	0.28	0.08	0.09	0.1	0.24							Na_2O	0.01	Na_2O	0	Na_2O	11.99	11.78	12.03	8.63
K_2O	10.65	10.66	10.81	11.61	10.73	Si	6.37	5.19	5.54	6.28	5.58	K_2O	9.95	H_2O	1.94	K_2O	0.04	0.06	0.05	0.13
BaO	0.29	0.14	0.16	0.16	0	Al iv	1.63	2.81	2.46	1.72	2.42	BaO	0.21	Total	99.86	BaO	0.02	0.02	0	0.01
H_2O	4.61	4.42	4.64	4.57	4.42	sum4	8	8	8	8	8	H_2O	3.92			Total	100.03	100.82	99.89	101.6
Total	101.42	99.27	101.76	102.97	98.33	Al vi	3.99	2.6	2.3	3.35	2.51	Total	100.3	Si	2.96					
						Ti	0	0	0	0	0			Ti	0	Si	2.97	3.01	2.98	2.72
Si	6.46	6.76	6.72	6.44	6.59	Fe2+	1.13	5.74	5.68	1.76	4.76	Si	2.72	Al	2.71	Al	1.02	0.99	1.01	1.27
Al iv	1.54	1.24	1.28	1.56	1.41	Mn	0.01	0.07	0.14	0.06	0.1	Al iv	1.28	Cr	0	Fe3	0	0	0	0.01
sum4	8	8	8	8	8	Mg	5.69	3.7	3.95	6.01	4.58	Ti	0.16	Fe3	0.33	Ti	0	0	0	0
Al vi	3.49	2.87	3.23	2.82	3	sum6	10.82	12.11	12.07	11.18	11.96	Al vi	0.29	Mg	0.01	su1	3.99	4	3.99	4
Ti	0	0.02	0	0.02	0.01	H	16	16	16	16	16	Fe2	1.37	sum6	3.05	Ba	0	0	0	0
Fe2+	0.1	0.43	0.09	0.02	0.13	Compo-sitions						Fe3	0	Ca	2.01	Ca	0.01	0.01	0.01	0.27

								9	7		9		2						0	0.73
Mn	0	0.01	0	0.01	0.01	Mg#	0.83	0.39	0.41	0.77	0.49	Mg	0.99	sum8	2.01	K	0	0	0	0.01
Mg	0.43	0.64	0.69	0.75	0.76	Fe#	0.17	0.61	0.59	0.23	0.51	sum6	2.83	H	1	su2	1.03	1	1.03	1.01
sum6	4.02	4.1	4.02	4.1	4.1							Ca	0	Compo-sitions		Compo-nents				
Ca	0.01	0	0	0	0							Na	0	Ps [Fe/(Al+Fe)]	0.11	Anorthite	0.01	0.01	0.01	0.27
Ba	0.01	0.01	0.01	0.01	0							K	0.97			High Albite	0.99	0.99	0.99	0.73
Na	0.07	0.02	0.02	0.03	0.01							Ba	0.01			K Feldspar	0	0	0	0.01
K	1.77	1.85	1.78	1.95	1.86							sum8	0.98							
sum8	1.86	1.88	1.82	1.98	1.87							H	2							
H	4	4	4	4	4							Compo-sitions								
Components												xAl	0.15							
Ms	0.7	0.51	0.61	0.57	0.6							Mg#	0.12							
Wm_Phl	0.01	0.05	0.01	0.05	0.05															
Al_Cel	0.2	0.23	0.32	0.22	0.25															
Fe_Al_Cel	0.04	0.15	0.04	0.01	0.04															
Pg	0.04	0.01	0.01	0.01	0.01															
Ti_Mn_Ca_Wm	0.01	0.05	0.01	0.14	0.05															
xOH	1	1	1	1	1															

Abbreviations: Ms - muscovite; Wm - white mica; Phl - phlogopite; Cel - celadonite; Pg - paragonite; Ps - pistacite; Structural formulae and various parameters (mainly molar fractions X of end member components) were calculated using the CALCMIN software (Brandelik, 2009) as follows: biotite O= 11, all Fe is divalent; white mica valences = 42, cations without interlayer cations ≤12.1; chlorite O= 28, all Fe is divalent; feldspar O=8; ilmenite O= 3, cations = 2.

Table 6; Modal (mod) and calculated (calc) composition of the samples analyzed for P-T pseudosection modeling showing interpreted P and T conditions. Abbreviations: Q – quartz; Pl – plagioclase; Kfs – alkaline feldspar; Wm – white mica; Bt – biotite; Ep – epidote; Tt – titanite; Op – opaques; Stlp – stilpnomelane; Cpx – clinopyroxene.

	FC1749		**FC1757**		**FC1723**		**FC1727**	
Mineral	Mod	Calc	Mod	Calc	Mod	Calc	Mod	Calc
Q	55	46	55	55	55	55	50	42
Pl	25	27	25	19.5	4	0.5	25	30
Kfs							5	7
Wm	15	16	10	7	30	31	15	13
Chl	5	3	4	3	10	10	5	2
Bt			5	2				
Ep			1	5	1			
Tt		0.1		0.5				0.2
Op	tr.		tr.		tr.		tr.	
Stlp		1						

water	6.7	8	3	5.4
P (kbar)	3.5	5.5	6	3.8
T (C)	230	440	450	330

1.25

Figure 1: A) Simplified geological map of the southern Patagonian and Fuegian Andes, modified after SERNAGEOMIN (2003). Gray box indicates the study area (detail in Fig. 2) in the region of Seno Skyring and Seno Otway, and the location of cross section A-A'-A'' of Isla Riesco: B) geological cross section interpreted from 2-D seismic lines by ENAP. Abbreviations: IR - Isla Riesco; CMSZ - *Canal de las Montañas Shear Zone* (Calderón et al., 2012); ETT - *Eastern Tobífera Thrust*; LPT - *La Pera Thrust*; RT - *Rocallosa Thrust*; MFSZ - *Magallanes-Fagnano Shear Zone*; the front of the MFTB (Magallanes Fold-and-Thrust Belt) is defined in Fosdick et al. (2011).

Figure 2: Geological map of the study area modified after SERNAGEOMIN (2003) and Betka (2013). Sample locations for rock samples collected for P-T pseudosection modeling are shown in purple hexagons with their respective field code. The sample locations of new geochronologic analyses with SHRIMP zircon U-Pb and $^{40}Ar/^{39}Ar$ in white mica are shown in the hexagons containing the respective mean ages in millions of years ago (Ma) and the field code is below. Cross sections of the Isla Riesco A-A'-A'', Canal Gajardo X-X', and Estero Wickham Y-Y' are shown in Fig. 1b, 3a and 3b, respectively.

Figure 3: Simplified geologic cross sections and structural data from the Patagonian Andes (refer to Fig. 2 for locations): A) Canal Gajardo (X-X') and B) Estero Wickham (Y-Y') modified after Haras bouk (2002) and Betka et al. (2015). Structural data from volcano-sedimentary bedding, metamorphic foliations, fold axes and axial planes are portrayed in stereographic projections above the respective sectors: A1) western and central areas of Canal Gajardo; A2) eastern area of Canal Gajardo; B1) western area of Canal Jerónimo and Estero Wickham; B2) northern area of Estero Wickham. The analyzed rock samples for P-T pseudosection modeling are shown in purple hexagons with their respective field code. The schematic location of new geochronologic analyses with SHRIMP zircon U-Pb and $^{40}Ar/^{39}Ar$ in white mica are shown in the hexagons containing the respective mean ages in millions of years ago (Ma).

Figure 4: Field photographs and photomicrographs of the mylonitic rocks of Tobífera Fm. in the hanging wall of the *Eastern Tobífera Thrust* at Estero Wickham: A) internal thrust contact within the folded Tobífera Fm.; B) photomicrograph of oriented thin section of silicic metatuff (FC1727, plane polarized light) showing the mylonitic S-C-type foliation (S_1*) in micaceous domains, and quartz and feldspar porphyroclasts with sigma-shaped strain shadows; C) photomicrograph of detail at sample FC1727 (crossed polarized light) showing ruptured plagioclase and sigma-shaped alkali feldspar, truncated by mica-rich cleavage domains of S_1*. D) Shale-rich intercalations within Tobífera Fm. in the foot wall of the thrust fault showed in A, cm-thick sandy layers are boudinaged and folded, an internal S_1* mylonitic foliation is oblique to the bedding S_0; E) photomicrograph of mylonitic metapelite (FC1728, plane polarized light) showing the S_1* mylonitic foliation, plagioclase and quartz porphyroclasts have sigma shapes and can be recrystallized to subgrains (SG).

Figure 5: Photomicrographs of representative lithologies of the *Western Domain* of the MFTB: A) metapelitic schist of the pre-Jurassic basement (FC1721, crossed polarized light) with two oblique preferential planes suggesting a S-C-type mylonitic foliation with shear sense to the northeast; sigmoidal microlithons of quartz show undulose extinction and subgrains with core-mantle texture; B) foliated metabasalt of the *Sarmiento Ophiolitic Complex* (FC1765, crossed polarized light) with the S_1* schistosity defined by cleavage domains of chlorite with sigmoidal geometries that suggest shear sense to the northeast; C) mylonitic silicic metatuff of the Tobífera Fm. (FC1749, crossed polarized light) with cleavage domains of white mica defining the S_1* schistosity, quartz porphyroclasts are ruptured and displaced with strain shadows of quartz and opaques suggesting shear sense to the northeast; D) mylonitic metapelite of the Tobífera Fm. (FC1750, crossed polarized light) with porphyroclasts of quartz and opaques with asymmetric strain fringes of quartz, and fragmented by domino-type structures suggesting shear sense to the northeast; E) metapsammopelite of the Zapata Fm. (FC1757, crossed polarized light) showing the folded relict foliation (S_1*) defined by quartz with bulging and subgrain rotation, it is overprinted by contact metamorphism that is characterized by non-oriented white mica, biotite, chlorite, and plagioclase; F) zoom in the decussed biotite and white mica of sample FC1757.

Figure 6: SHRIMP zircon U-Pb results: A) Tera-Wasserburg concordia plot, age versus relative probability diagram, weighted mean age, and demonstrative analyzed zircon grains from mylonitic silicic metatuff of the Tobífera Fm. (FC1727); B) Age versus relative probability diagram, Tera-Wasserburg concordia plot, and representative analyzed zircon grains from the metapsammopelite of Zapata Fm. (FC1754), and C) age versus relative probability diagram for the Cretaceous ages; D) Tera-Wasserburg concordia plot, age versus relative probability diagram with weighted mean age, and analyzed zircon grains from quartz-diorite (FC1759) intruding thrust sheets of Canal Gajardo.

Figure 7: A) Photomicrograph of mylonitic metapelite of Zapata Fm. (SHP141) with mats of phengite (crossed polarized light), and B) diagram of *in-situ* $^{40}Ar/^{39}Ar$ dates with errors reported at the 1 σ level, the light gray bar (spot 7, Table 3) is considered an outlier.

Figure 8: Diagrams of mineral chemical classification based on major element composition of white mica, chlorite, and feldspar, measured with the EPMA in samples FC1723. FC1727. FC1749 and SHP141: A) White mica solid solutions celadonite-

pl ersus Si (a.p.f.u.) (Foster. 1962); C) feldspar triangular diagram based on the alkali ratio X_{Na} with Anorthite – Albite – Orthoclase end members (Deer et al., 1963).

Figure 9: Calculated P-T pseudosections and selected isopleths for the analyzed samples with ellipses indicating the estimated P-T field of regional metamorphism: A) mylonitic silicic metatuff (FC1749,Tobífera Fm.) - P-T at ~ 3-4 kbar and ~ 210-250°C; B) metapsammopelite (FC1757, Zapata Fm.) - P-T at ~ 5-6 kbar and ~430-460°C, the maximum T may be related with contact metamorphism; .C) mylonitic silicic metatuff (FC1723, Tobífera Fm.) - P-T at ~ - 5.3-6.3 kbar and ~ 420-460°C; D) mylonitic silicic metatuff (FC1727, Tobífera Fm.) - P-T at ~ 3-4 kbar and ~ 300-340°C. Mineral abbreviations: Wm - white mica; Chl - chlorite; Kf - alkali feldspar; Pl - plagioclase; Cp - clinopyroxene; Ep - epidote; St - stilpnomelane; Bt - biotite; Tt - titanite; Gt - garnet; Q - quartz; Act - actinolite; Lw - lawsonite; Stb - stilbite; Anl - analcite; Ilm - ilmenite; Fc - carpholite; Mt - magnetite; Hm - hematite; Lmt - laumontite; Zo - zoisite; Ru - rutile; And - andalusite; An - annite; Ka - kaolinite; Pu - pumpellyite; Pr - prehnite; Pnt - pyrophanite; Pxm - pyroxmangite; W - water.

Figure 10: Schematic SW-NE geologic cross sections summarizing the proposed tectonic evolution of the RVB and the Patagonian orogenic belt between the latitudes 52 to 54°S. Respective paleogeographic reconstructions from Dalziel et al. (2013) and Poblete et al. (2016) are shown on the right hand side with the approximated location of cross-sections indicated by a black bold line. Abbreviations: AP – Antarctic Peninsula. KC – Kalahari Craton, MAB – Magallanes-Austral Basin, M/FI – Malvinas/Falkland Islands, RPC – Rio de la Plata Craton, SG: South Georgia Island, SO: South Orkney Island, Pt – Patagonia, RVB – Rocas Verdes Basin. A) Late Jurassic to Early Cretaceous phases of opening of RVB due to rifting and coeval silicic volcanism of the Tobífera Fm.; seafloor spreading of the Rocas Verdes oceanic lithosphere; and the hemipelagic and siliciclastic sedimentation of the Zapata Fm. from sources including the incipient *South Patagonian Batholith*, pre-Jurassic basement horsts, and Tobífera topographic highs (*ages from Calderón et al., 2007). The dashed line in the paleogeographic reconstruction is the approximated continental boundary between South America and Africa before the opening of the Atlantic Ocean, which starts at ca. 130 as well as the Weddel Sea opening. B) Late Cretaceous pre-Campanian underthrusting of the oceanic and continental lithosphere of the RVB beneath the parautochthonous magmatic arc. During this time, a northeast verging underthrusted crustal stack developed, reaching ~ 23 km depth (as recorded by samples that underwent greenschist-facies metamorphism). Offscraping of ophiolitic slices occurred along shear zones with fluids from dehydrated buried rocks. The development of S_1* foliation formed due to shearing in ductile shear zones and its crenulation within inner zones of the belt generated transposition by the S_2* foliation. In the paleogeographic reconstruction the yellow area represents the sediments of the Magallanes-Austral Basin, the Weddell Sea is opened and in a relatively quiet period. The Antarctic Peninsula and the South Georgia Island are separated from the South American continent. C) Campanian to early Oligocene phase of uplift and exhumation of the underthrusted crustal stack by of out-of-sequence thrusting and backthrusting within the RVB successions, the location of the Eastern Tobífera Thrust is approximated. Inversion of inherited normal faults account for imbrications with the pre-Jurassic basement and resulted in a thick-skinned arrangement of the *Western Domain* of the MFTB, which transferred deformation to the Upper Cretaceous units of the Magallanes-Austral Basin.

Highlights:

- U-Pb geochronologic constraints for the opening and closure of the Rocas Verdes Basin
- Pressure - temperature estimates of metamorphism in Tobífera and Zapata formations
- $^{40}Ar/^{39}Ar$ in phengite age of deformation within the Magallanes fold-and-thrust belt
- Cross sections and tectonic reconstruction of the Southernmost Patagonia